Efficient laminar flow control

Efficient laminar flow control

Gaspare Li Causi,[*,†] Enrico Amico, and Jacopo Serpieri
Department of Mechanical and Aerospace Engineering, Politecnico di Torino, Turin, Italy

(Received 22 October 2025; accepted 27 January 2026; published 5 March 2026)

Research studies conducted over the years have demonstrated that wall suction is a highly effective laminar flow control (LFC) technique to delay laminar to turbulent transition. In this work, we investigated efficient LFC configurations. These are evaluated both in terms of the drag and power exerted by the flow and demanded by the LFC system. To derive the LFC power, the literature analyses on drag reduction for turbulent flows were adapted for the LFC applications hereby considered, leading to the identification of the relevant power-contributing terms. Two methods, originally developed to predict the transition location for uncontrolled flows, were employed to explore LFC configurations. These are specifically the so-called e^N method, derived from the linear stability theory, and the γ-Re$_\theta$ model. Only the γ-Re$_\theta$ approach gave more robust results for LFC applications. As such, it was embedded in an iterative framework exploiting Bayesian optimization to find the most beneficial configurations, for uniform suction LFC, to control the archetypal, bidimensional, and incompressible flat plate flow. Overall, 700 configurations were explored. Efficient LFC configurations were found with the optimal configuration delivering 34% of total power saving. This study, establishing a robust and computationally affordable methodology, while developing the power budget breakdown, paves the way for efficient LFC for aeronautical flows, possibly considering nonuniform suction, pressure gradients, surface curvature, the third spatial direction as well as flows at different Reynolds and Mach numbers.

DOI: 10.1103/sq42-dlzp

I. INTRODUCTION

A. Context

The continuous and rapid increase in air traffic, coupled with the pressing need for environmental sustainability, has sparked renewed interest in flow control techniques, particularly those focused on drag reduction [1]. In fact, friction drag overcomes 50% of the total drag on commercial airliners.

Laminar flow control (LFC) represents a specific subset within the broader category of flow control methods, thoroughly reviewed by Joslin [2] and further updated by Beck *et al.* [1], Krishnan *et al.* [3], and Svorcan *et al.* [4]. LFC is an active flow control technique, i.e., considers energy expenditure for its operation, that aims to increase the portion of laminar flow over the flow-wetted surfaces. The reason for doing so resides on the fact that turbulent boundary layer (BL) flows cause high values of wall shear stresses, considerably greater than the laminar counterpart. Given that

[*]Contact author: gaspare.licausi@polito.it
[†]Also at SISSA, International School for Advanced Studies, Trieste, Italy.

friction drag contributes to nearly half of the total drag to be overcome by an airliner during cruise flight, delaying laminar to turbulent transition can much reduce drag, costs, and pollution [5].

The primary LFC technique, extensively tested since the 1930s in laboratory setups and numerical simulations, consists in applying a steady suction, through porous plates, to boundary layer flows (e.g., Refs. [6–10]). Over the years, alternative LFC approaches, such as wall heating and cooling or based on conditioning the BL with wall mounted plasma actuators or Lorentz-force actuators, have also been investigated with the aim of controlling the transition mechanisms or of reducing friction drag (e.g., Refs. [11–20]). Nevertheless, the most technologically available LFC method to date continues to be wall suction [2].

In addition to LFC, another form of passive flow transition control, known as natural flow control (NFC), involves shaping the aerodynamic bodies to induce weaker adverse pressure gradients on the surrounding flow, as these are, for incompressible bidimensional flows, the major contributors to the boundary layer instability mechanisms causing the flow turbulent breakdown.

While NFC is effective in reducing drag at the design conditions, the airfoil/wing performances might deteriorate in off-design conditions. Integrating LFC with NFC led to the development of hybrid laminar flow control (HLFC), which showed convincing results (see the review article in Ref. [3]).

For low levels of free-stream turbulence, and for two-dimensional incompressible flows over smooth walls, the BL transition process is dominated by the amplification of Tollmien–Schlichting (TS) waves [21]. This phenomenon, within the limits of non considering interactions among the different modes, can be well-described by local, parallel flow theories as the linear stability theory (LST) or by more sophisticated approaches as, e.g., linear/nonlinear parabolized stability equations, triple deck theory, (bi)global stability theory [22]. During the receptivity stage, the energy carried by disturbances such as noise, mechanical vibrations, or turbulence fluctuations penetrate the boundary layer [23]. LST fairly elucidates the early stages of the BL flow stability where these perturbations propagate within the boundary layer being either damped or amplified. Nevertheless, LST coupled with the so-called e^N method [24,25], is a much adopted mean to estimate the BL stability given its relatively easier implementation and faster evaluation.

B. Laminar flow control

At relatively low Reynolds numbers, LFC is an effective and efficient technique for drag reduction. By examining the suction stabilizing effect within the framework of LST, it has been observed that even small values of suction velocity can significantly increase the critical Reynolds number, which is the streamwise-length-scaled Reynolds number at which the transitional BL perturbations amplify for the very first time [21]. The LFC stabilization of the BL flow is attributed to the alteration of the mean flow profile due to the applied wall suction (see the pioneering work in Ref. [26]). The resulting fuller profile exhibits enhanced stability with respect to instabilities as TS waves for two-dimensional flows and cross-flow instability modes for three-dimensional flows (see the review articles in Refs. [27,28]).

Although the capability of suction was already explored by Prandtl [21], the first systematic experiments of wall suction flow control on a flat plate were performed by Reynolds and Saric [7]. Using a low turbulence wind tunnel, BL hot-wire (HW) measurements were conducted to investigate the stabilizing effect of suction control over a flat plate BL. The flat plate was equipped with two porous panels, each consisting of 15 independent strips, through which a wall-normal velocity was imposed at different streamwise positions and extending for different streamwise lengths. Perturbations were introduced in the boundary layer by means of a vibrating ribbon, and their amplitude was tracked all over the plate with the HW scans. The evolution of the amplitude of the induced mode along the streamwise coordinate was, therefore, investigated under different suction configurations. The evaluation of each configuration's authority in controlling and containing the disturbance growth was investigated, taking care of keeping the same sucked mass flow across the different suction configurations. In this study, the measured disturbance amplitudes were compared

to the triple deck theory proposed in Ref. [29]. The experiments revealed that the perturbations amplitude displayed uniform qualitative behavior across all analyzed configurations. Furthermore, it was found that the most effective suction occurs when it is applied between the first point of disturbance instability and the point of maximum amplification rate. While the qualitative trend predicted by the triple-deck theory aligned with the experimental data, noticeable quantitative discrepancies were observed, with predicted amplitudes consistently smaller than the measured values.

Fransson and Alfredsson [8] conducted a thorough investigation encompassing theoretical, numerical, and experimental efforts to analyze the impact of suction on BL stability. They examined the impact of uniform suction on a flat plate and ensured that an asymptotic suction boundary layer profile was achieved far downstream. By inducing TS waves using alternating suction and blowing through two slots, they observed the evolution of disturbances within the asymptotic suction region. Detailed comparisons between LST-predicted and experimental results demonstrated that LST is a valid model for representing the evolution of perturbations in a boundary layer without suction control. However, when assessing the evolution of perturbations over the asymptotic suction region, discrepancies between theory and experiments emerged. The distribution of phase and velocity perturbations became scattered immediately downstream of the location where the perturbations were introduced. Furthermore, LST predicted disturbances' decay rates significantly larger than the measured values, suggesting an overestimation of the LFC effectiveness by LST.

A recent experimental campaign on suction was conducted by Corelli Grappadelli *et al.* [9]. Unlike previous studies that combined theoretical and experimental considerations, this study mainly produced a large set of experimental data. Using infrared thermography, they tracked the transition displacement as a function of suction intensity. Suction was applied through two different porous media, fixed at a location immediately downstream of the flat plate leading edge (LE). After establishing a relationship between the point of natural transition and the Reynolds number, the effects of suction at five different Reynolds numbers were explored.

Over the past years, in flight LFC tests were carried out too, usually considering mature aircraft models equipped with ad hoc wing or vertical stabilizer LFC glove (e.g., Refs. [30–32]).

The design of the suction system for LFC requires careful consideration. Suction is achieved through discrete, laser-drilled surface perforations, typically ranging from tens to hundreds of micrometers. The flow field around each micro-perforation is intricate and highly three-dimensional. These perforations can create counter-rotating streamwise vortices, which can be stable or unstable depending on the flow conditions (e.g., Refs. [10,33,34]). Moreover, these vortices can lead to highly distorted, inflectional, and unstable streamwise velocity profiles (e.g., Refs. [34,35]). These phenomena are collectively known in the literature as over-suction effects, which, contrary to the objectives of LFC, can promote earlier transition.

The majority of the existing literature on LFC primarily focuses on the transition delay associated with boundary layer suction. However, merely shifting the transition location is insufficient to demonstrate the effectiveness of LFC unless it also results in an overall power reduction. While a decrease in power consumption typically suggests a transition delay, the reverse is not necessarily true. If the energy saved by extending the laminar flow region is less than the additional power required to operate the suction system, then LFC could prove detrimental, ultimately leading to an increase in overall power consumption.

C. Efficient active flow control

The most recent studies on active flow control have started taking into account not only the benefits of actuation but also the so called cost of actuation [36–41]. Nevertheless, we should highlight that these studies considered active flow control, based on wall transpiration, for the sake of turbulent skin friction drag reduction. Already Rioual *et al.* [42] pointed out that, in an active flow control scenario, the power can be decomposed into the sum of 3 different terms, which are: the power provided by the propulsive system to win the body's drag, the power needed by the pump

to actuate the suction control and, last, the power that can be recovered by expelling the sucked mass flow to generate some amount of thrust. The overall drag coefficient can be understood as comprising the conventional body drag—slightly different from the classical airfoil drag without mass suction—augmented by the normalized pump power expressed as a drag coefficient, and including a negative drag term associated with the thrust generated by expelling the ingested mass flow at a specific velocity.

A power budget oriented study, but applied to LFC, is presented by Beck *et al.* [1], who proposed to consider the suction related power by converting this power in terms of additional drag coefficients. This new drag formulation was adopted later in Ref. [38] in the context of turbulent boundary layer (TBL) control for uniform blowing and suction. Here, the new perspective on power showed interesting results. Fahland *et al.* [39] dedicated their most recent work to emphasize the significance of utilizing the appropriate drag formulation when assessing the performance of active flow control strategies that involve the transpiration of mass through the boundary of a controlled body. By conducting both compressible and incompressible RANS simulations on an airfoil, they demonstrated how the body drag—calculated by integrating the stresses over the airfoil's boundary—differs from the wake survey drag, often used as a surrogate measure in experimental setups. This discrepancy between the body drag and wake survey drag highlights the impact of boundary layer control. While reductions in body drag may be observed in certain cases compared to the uncontrolled scenario, the wake survey drag consistently exceeds that of the uncontrolled case. Consequently, when considering the cost of actuation, none of the TBL control configurations investigated resulted in a decrease in total power consumption. Notably, since the wake survey drag accounts for the actuation cost in the case of blowing, it was referred to as inclusive drag.

Mallor *et al.* [41] studied optimal BL suction configurations to enhance the aerodynamic efficiency of a NACA wing profile under both cruise conditions and high-lift scenarios. Three efficiency metrics were evaluated: the first ignored the energy penalties associated with suction, the second included an idealized actuation cost, assuming no energy losses, and the third took into account the efficiency of the required pumps and turbines, as well as the losses in the system's pipelines. Notably, the outcomes derived from these three efficiency metrics varied significantly. Specifically, while neglecting power costs suggested that active flow control could substantially improve airfoil performance, these benefits diminished when the energy required to operate the control mechanisms was considered. The most critical finding was that active turbulent boundary layer control proved largely ineffective during cruise conditions but demonstrated a pronounced ability to enhance performance in high-lift scenarios.

D. Current study

In this study, our primary objective is to explore efficient, uniform suction, LFC configurations on a flat plate, bidimensional, incompressible flow. While the choice of this flow facilitates the implementation of the proposed study, given the simpler boundary layer transition mechanisms at play, it leads to more general conclusions, as the flat plate, and the related flow are not influenced by specific geometries. Clearly, the proposed analysis and methodology could be extended to more realistic, and likely more specific, flows in the future.

Then, drawing on recent advancements in turbulent skin friction control, we formulated the LFC problem in terms of power efficiency, breaking down all the relevant contributions and analyzing their evolution under LFC. Flow control efficiency was partially addressed by Rioual *et al.* [42], who provided a semi-analytical equation for calculating the overall power of a flat plate boundary layer. We built upon that work by replacing the e^N transition prediction method employed in Ref. [42] with what we demonstrated, through a detailed comparison with the experimental data from Ref. [9], to be a more accurate transition model; namely, the γ-Re_θ model [43,44].

Finally, we set up an optimization framework based on Bayesian optimization (BO) and fast fluid dynamics solvers to explore efficient LFC configurations. The found optimal configuration delivers an overall power reduction overcoming 34% compared to the unforced flow.

The remainder of the paper is organized as follows. In Sec. II, the methodology followed in this study is described. Section III is devoted to the description of the results of this study, which are then further discussed in Sec. IV. Finally, the conclusions of this work are reported in Sec. V. Furthermore, an assessment of the LST-LFC solver is presented in Appendix A, while a simplified description of the BO formulation is reported in Appendix B.

II. METHODOLOGY

In this section, we first describe the two main approaches followed to evaluate the effect of LFC: LST with the e^N method and CFD leveraging on the γ-Re_θ transition model; then we expose the optimization framework and finally we present the power budget analysis.

A. Linear stability theory for laminar flow control

LST is based upon the solution of the Orr-Sommerfeld (OS) equation, which, mathematically speaking, represents an eigenvalue problem. The derivation of this equation begins with the linearization of the Navier-Stokes equations around a base flow which can be the time-averaged flow field (here denoted with capital letter $\boldsymbol{U}$, where in bold we report vectors), which is assumed to be two-dimensional, steady, incompressible, and locally parallel ($\boldsymbol{U} = [U(y),\ 0,\ 0]$, where $U(y)$ represents the streamwise velocity component and y the wall normal coordinate). Upon this base flow, two-dimensional wave-like perturbations, are superimposed. Depending on whether the amplitude of these perturbations is modeled to be amplified or dampened over time or along spatial coordinates, two different LST formulations emerge: the temporal and spatial approaches. Following the temporal approach leads to a simpler and less expensive eigenvalue problem to be solved. However, the spatial approach encompasses a more useful description of the perturbation evolution, having as a disadvantage a complex mathematical solution strategy.

By solving the eigenvalue problem, a functional relationship is established between the local velocity profile, its curvature, a local-length-based Reynolds number (for example, considering the local displacement thickness $\delta^*(x)$: Re_{δ^*}), the angular frequency ω, and the wave number α. This functional relationship can be described by

$$f(U,\ D^2U,\ \alpha,\ \omega,\ \mathrm{Re}_{\delta^*}) = 0, \tag{1}$$

where the D^2 operator represents the second order derivative along the wall normal direction y. α is a complex number, made of a real part, associated with the wave number of the mode and an imaginary part,which, becoming a real argument of the exponential function in Eq. (5), is to be deemed as the modal amplification/damping factor.

When wall suction is applied, the hypothesis of locally parallel flow no longer holds due to the appearance of an intense wall normal velocity component. A novel base flow formulation is thus required: $\boldsymbol{U} = (U(y),\ V(y),\ 0)$. Following Reynolds' decomposition, is then possible to decompose pressure and velocity fields as the sum of a base flow (capital letters) plus the fluctuating part (indicated with the apex):

$$u_i(x,\ y,\ t) = \underbrace{U_i(y)}_{\sim 1} + \underbrace{u_i'(x,\ y,\ t)}_{\sim \varepsilon}, \qquad i = 1,\ 2, \tag{2}$$

$$p(x,\ y,\ t) = \underbrace{P(y)}_{\sim 1} + \underbrace{p'(x,\ y,\ t)}_{\sim \varepsilon}, \tag{3}$$

where t is time and x the streamwise coordinate. Assuming the fluctuations to be of much lower magnitude than the base flow ($\varepsilon \ll 1$), it is possible to linearize the system of equations:

$$\frac{\partial u_i}{\partial x_i} = 0,$$

$$u_j \frac{\partial u_i}{\partial x_j} = -\frac{\partial p}{\partial x_i} + \frac{1}{\mathrm{Re}} \frac{\partial^2 u_i}{\partial x_j \partial x_j}. \tag{4}$$

The terms in the previous equations are dimensionless quantities. This holds for the whole section, unless otherwise specified. The velocities u_i are normalized with the BL edge velocity $U_e(x)$ (equivalent to U_∞ for the flat plate flow), while the spatial coordinates x_i are divided by the local value of the BL displacement thickness $\delta^*(x)$. The pressure p is normalized by $\rho U_e(x)^2$, where ρ is the flow density. The Reynolds number is therefore $\mathrm{Re}(x) = U_e(x)\delta^*(x)/\nu$.

Following the linearization and the normal mode approach, the flowfield perturbations are described as independent Fourier modes whose ansatz is the following:

$$v'(x,\ y,\ t) = \hat{v}(y)\, e^{i(\alpha x - \omega t)}, \tag{5}$$

where ω is the angular frequency of the mode, while α is a complex number: $\alpha = \alpha_r + i\alpha_i$, and where α_r is the wave number, while $-\alpha_i$ is the amplification rate. If the amplification rate is positive ($-\alpha_i > 0$), the mode is unstable and its amplitude will growth as x increases. The opposite happens when the amplification rate is negative ($-\alpha_i < 0$): the mode is stable and its amplitude will be damped as the perturbation moves downstream.

When considering suction, the modified OS equation becomes

$$\left[(i(\alpha U - \omega) + V')(D^2 - \alpha^2) + V(D^3 - \alpha^2 D) - i\alpha U'' - \frac{1}{\mathrm{Re}}(D^4 - 2\alpha^2 D^2 + \alpha^4)\right]\widehat{v} = 0, \tag{6}$$

where, similar to Eq. (1), D^3 indicates the third order wall-normal derivative and U'' the curvature of the velocity profile. The equation is identical to the one mentioned in Ref. [8], with the exception of the term V'. This term is absent in their equation because in the asymptotic suction profile, $V(y) = V_w =$ constant, rendering it unnecessary. A validation of our LST solver against the results of Ref. [8] is presented in Appendix A. Our research aims to analyze the stability of not only the potential asymptotic region but also the transient region, which compelled us to introduce V' to account for situations where it may not be zero in the initial segment where suction is applied. Eq. (6) can still be written as an eigenvalue problem, where the eigenvalue α appears non linearly.

To solve this equation, different approaches have been proposed. The first is the "shooting method" with orthonormalization, as described in Ref. [45]. This method is effective when a good initial approximation of the solution is available, and it involves an iterative algorithm to integrate the approximated solution over the entire domain until the boundary conditions coincide with those imposed. However, the convergence of this method heavily depends on the quality of the initial estimate. In situations where such an estimate is unavailable, the method introduced in Ref. [46], commonly known as the "companion matrix method," is preferred. This method is, in fact, independent of the initial solution estimate. To reduce the dimension of the final companion matrix the transformation proposed by Haj-Hariri [47] was implemented:

$$\widehat{v}(y) = \widehat{V}(y)\, e^{-\alpha y}. \tag{7}$$

The y coordinate was discretized with a distribution of Chebychev points:

$$\eta_j = \cos\left(j\frac{\pi}{N_c}\right); \quad -1 \leqslant \eta_j \leqslant 1; \quad j = 0, 1, \ldots N_c, \tag{8}$$

with $N_c + 1$ being the number of Chebychev nodes. Since the coordinate y is upper-unbounded, a transformation capable of mapping the interval $[-1,\ 1]$ to $[0,\ y_\infty]$ is required. Motsa and Makukula [48] proposed the following transformation:

$$y = y_\infty \frac{1+\eta}{2}. \tag{9}$$

TABLE I. Convergence study for the OS spectrum's dominant root at $\omega = 0.08$ for two baseflows.

N_c	$\mathrm{Re}_{\delta^*} = 400$	$\mathrm{Re}_{\delta^*} = 800$
20	$2.103152 \times 10^{-01} + \mathrm{i}9.618464 \times 10^{-03}$	$2.231912 \times 10^{-01} - \mathrm{i}4.140604 \times 10^{-03}$
40	$2.097405 \times 10^{-01} + \mathrm{i}1.080762 \times 10^{-02}$	$2.247430 \times 10^{-01} - \mathrm{i}3.145444 \times 10^{-03}$
80	$2.097404 \times 10^{-01} + \mathrm{i}1.080755 \times 10^{-02}$	$2.247434 \times 10^{-01} - \mathrm{i}3.145770 \times 10^{-03}$
160	$2.097400 \times 10^{-01} + \mathrm{i}1.080753 \times 10^{-02}$	$2.247431 \times 10^{-01} - \mathrm{i}3.145795 \times 10^{-03}$

The independent variables (here generally referred as $q(y)$) were approximated by Lagrange interpolating polynomials $l_k(y)$:

$$l_k(y) = \prod_{i=0}^{N} \frac{y - y_i}{y_k - y_i}, \tag{10}$$

$$q^L(y) = \sum_{i=0}^{N} q_i \, l_i(y). \tag{11}$$

In Eq. (11), $q^L(y)$ denotes the Lagrange polynomial approximation of $q(y)$, while $q_i = q(y_i)$ indicates the values assumed by $q(y)$ on the ith node. For further detail about the equation discretization and definition of the Lagrange differentiation matrix, refer to Ref. [49].

The output of the LST solver consists of $N_c + 1$ pairs of eigenvalues (α) and eigenfunctions [$\hat{v}(y)$]. Most of these are spurious solutions of the eigenvalue problem, necessitating a filtering stage to isolate the physically relevant pairs. After the filtering process, a set of plausible eigenvalues remains, each potentially determining different amplification rates for a given mode. The key eigenvalue in the transition process is the dominant root, which corresponds to the physical eigenvalue with the largest amplification factor $-\alpha_i$. An independence study was conducted to ensure that the dominant root is independent from the number of Chebyshev collocation points (see Table I), and $N_c = 80$ was selected for the subsequent calculations.

When the amplitude of the disturbances becomes significant, the base velocity profile deviates from the laminar state. Building on this physical intuition, Van Ingen [24] and, independently and simultaneously, Smith and Gamberoni [25] proposed the e^N method for transition prediction. For each ω mode, the associated amplification/damping factor $n(\omega,\ x)$ is estimated as

$$n(\omega,\ x) = \log\left(\frac{a(\omega,\ x)}{a_0(\omega)}\right) = \int_{x_0(\omega)}^{x} -\alpha_i(\omega,\ x)\, dx, \tag{12}$$

where $a_0 = a(\omega,\ x_0)$ is the perturbation amplitude at the location x_0 where the mode ω begins to be amplified. From the envelope of the $n(\omega,\ x)$ curves, a single curve $N(x)$ is obtained as $N(x) = \max_\omega(n(\omega,\ x))$. According to this method, the transition is considered complete when a critical N factor (N_{cr}) is reached. N_{cr} needs to be estimated from ad hoc experimental campaigns.

TABLE II. Summary of the considered CFD BCs. ZG is the acronym for zero gradient.

BC	U	p	k	$\tilde{\omega}$	γ	Re_θ
Inlet	$(U_\infty,\ 0,\ 0)$	ZG	$5.42e-4$		1	1136.5
Outlet	ZG	0	ZG		ZG	ZG
Wall	$(0,\ 0,\ 0)$	ZG	0		ZG	ZG
Porous wall	$(0,\ v_w,\ 0)$	ZG	0		ZG	ZG
Symmetry up and down	ZG	ZG	ZG	ZG	ZG	ZG

TABLE III. Mesh characteristic parameters: the reference mesh size in the streamwise direction (Δx_{ref}); the number of nodes used to discretized the leading edge (N_{LE}); the height of the first boundary layer (BL) cell (h_f); the number of nodes discretized the BL (N_{BL}); the estimated transition point (x_t); the drag coefficient (c_d).

Refinement	Δx_{ref} [mm]	N_{LE}	h_f [μm]	N_{BL}	x_t [m]	$10^3\, c_d$
Fine	$2\sqrt{2}$	340	$2\sqrt{2}$	113	1.639	2.704
Medium	4	240	4	80	1.653	2.731
Coarse	$4\sqrt{2}$	170	$4\sqrt{2}$	57	1.428	2.791

B. Computational fluid dynamics

In this section, we describe the CFD approach followed in this study. The Langtry-Menter four-equation transitional SST model [43,44] for LFC flows implemented in OpenFOAM v2212 was exploited.

First, to assess the approach accuracy, the derived results were validated against the experimental data in Ref. [9]. In fact several parameters revealed to be crucial for the correct computation of laminar-transitional flows. The plate leading edge is one of these as it is the region where environmental disturbances, such as acoustic waves and free-stream turbulence, transfer their energy to perturbations within the boundary layer [50]. Moreover, the aft region of the leading edge induces an adverse pressure gradient, which contributes to the BL destabilization [51]. To ensure a fair comparison and accurate validation, a CFD simulation was carried out using the same leading edge geometry described in Corelli *et al.* (2021). The leading edge shape was explicitly defined by the control points of a fifth-order Bezier curve, resulting in a symmetrical profile.

The simulation took advantage of the symmetry of the problem with respect to the streamwise direction by investigating only half of the domain, thus reducing the computational cost. Figure 1 depicts the computational domain, along with the boundary names and the geometrical dimensions. The flat plate thickness is $t_{pl} = 70$ mm (half thickness $t_{pl}/2 = 35$ mm) while the LE length chord measures 450 mm and the flat plate length is 3600 mm for a total length of 4050 mm, which was chosen as reference length (L). The CFD domain inlet is a quarter circle with radius 1835 mm, corresponding to the domain height (H). The reference system features its origin at the downstream end of the leading edge (i.e., at the beginning of the flat geometry).

Suction is implemented by applying a uniform wall-normal velocity across the porous wall. Although, for the physical flow, the flow leaves the fluid domain over this boundary, a patch type *wall* was chosen to enable the application of the turbulence model. To mimic suction, the following

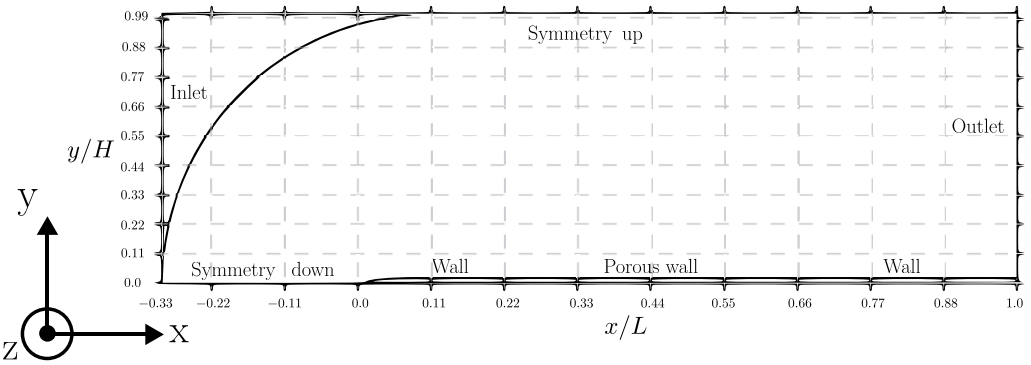

FIG. 1. Computational domain, with different zones and BCs and coordinates system.

TABLE IV. Numerical schemes employed for the CFD simulations (fvScheme file).

Term	OpenFOAM Keyword	Description
Time derivative	`steadyState`	Steady-state solver
Gradient (∇)	`Gauss linear`	Second-order central differencing
Convection ($\nabla\cdot$)	`bounded Gauss linearUpwind`	Second-order upwind (Bounded)
Diffusion (∇^2)	`Gauss linear corrected`	Central Diff. with nonorthogonal corr.
Interpolation	`linear`	Linear interpolation
Surface n. gradient	`corrected`	Explicit nonorthogonal correction

velocity boundary condition (BC) at the plate wall is adopted:

$$\boldsymbol{U}|_{y=0} = (0,\ v_w,\ 0), \tag{13}$$

where $v_w < 0$ ($v_w > 0$) denotes suction (blowing) scenarios. Throughout this paper, only negative values of v_w are retained.

The validity of this patch was tested against results produced by a BL equations solver and the theoretical solution of the asymptotic suction profile, which reads as

$$\frac{u(x,y)}{U_e(x)} = 1 - e^{\frac{v_w y}{\nu}}. \tag{14}$$

It is possible to find the numerical values of the BCs adopted in the simulations in Table II. The CFD profile agrees well both with the result of the BL solver and the asymptotic suction profile, demonstrating the possibility of coupling the suction boundary conditions with the turbulence model on the same boundary.

In their study, Corelli Grappadelli *et al.* [9] established a correlation between the transition point, denoted as x_t, and the Reynolds number ($\mathrm{Re}_L = \frac{U_\infty L}{\nu}$) across a wide range of Re_L. For now, our focus is on a specific Re_L value. The Re_L value we chose corresponds to the one for which the difference between C_q-x_t curve becomes minimal for the two different porous panels (see Fig. 14(a) in Ref. [9]). The corresponding free-stream velocity for this scenario is $U_\infty = 19$ m/s, with an assumed turbulence intensity of $Tu = 0.08\%$.

A fixed free-stream velocity value (U_∞, 0, 0) was prescribed as BC at the inlet, while a no-slip condition was imposed on the solid and porous wall. The symmetry and outlet regions featured a zero gradient velocity boundary condition. The outlet pressure is set to zero, and a null pressure gradient was applied to the other boundaries. Inlet boundary conditions for the turbulent model were calculated from the following relations:

$$k = \tfrac{3}{2}(Tu\,U_\infty)^2, \tag{15}$$

$$\tilde{\omega} = \frac{k}{\nu_T}, \tag{16}$$

where k is the turbulent kinetic energy and $\tilde{\omega}$ is the specific turbulence dissipation. The eddy viscosity ratio (ν_T/ν) is set to 1. Additionally, considering $T = Tu \times 100$, the inlet boundary condition for Re_θ is defined as in Ref. [52]:

$$\mathrm{Re}_\theta = \begin{cases} 1173.51 - 589.428\,T + 0.2196\,T^{-2}, & T \leqslant 1.3, \\ 331.50\,(T - 0.5658)^{0.671}, & T > 1.3. \end{cases} \tag{17}$$

Additional information about the numerical scheme adopted and the solver utilized to run the simulation is collected in the Tables IV and V.

The computational domain and mesh were generated using Gmsh. The simplicity of the computational domain makes it well-suited for structured mesh discretizations, leading to faster convergence [53].

TABLE V. CFD simulations convergence criteria and residual thresholds.

Variable	Solver	Residual threshold
Pressure (p)	GAMG	1×10^{-5}
Velocity ($\mathbf{U}$)	smoothSolver	1×10^{-6}
Turbulence (k, ω)	smoothSolver	1×10^{-4}
Transition (γ_{Int}, $\text{Re}_{\theta t}$)	smoothSolver	1×10^{-4}

To assess the solution convergence against the chosen discretization, three different grids were generated. These are hereon referred to as: Coarse, Medium, and Fine. These meshes were created with a constant height of the first cells from the wall, but they differ in the number of nodes in parallel and wall normal directions. The characteristic length of two subsequent meshes differs by a factor of $\sqrt{2}$ resulting in a doubling of the total mesh points from a grid to the subsequent. The thickness of the inflation layer was kept at $0.247\,L$ (0.1 m), which is greater than the estimated turbulent boundary layer thickness at the flat plate trailing edge (TE). The height of the first cell and the number of layers within the boundary layer are imposed. Outside the boundary layer, a progression rate of 1.1 is set.

To improve the resolution in the regions with the highest gradients, such as the LE and the porous wall, the x-characteristic mesh size (Δx_{ref}) was refined. Direct control over the element size along the x and y directions allows for greater authority over the mesh quality. Both the convergence study and subsequent optimization simulations were run until all variable residuals dropped below the thresholds reported in Table V.

The main detail and the results of the grid convergence study are presented in Table III and Fig. 2. Qualitative convergence is evident when examining the skin friction coefficient distributions for the three grids analyzed. While the transition from the coarse to the medium grid results in a significant shift in the friction coefficient curve, and consequently the transition point, further refinement (from the medium to the fine grid) has a negligible effect on the skin friction distribution. Similar observations can be made for the global quantity c_D listed in Table III. Therefore, for the optimization, the Medium grid is deemed as a good tradeoff between solution accuracy and computational costs and is thus the one selected.

C. Optimal LFC

Exploring the effect of the many LFC parameters toward finding efficient configurations requires some smart approach as the related parametric space can be large and the optimization functions (e.g., drag or power reduction) can be rather complex. Several approaches could be considered (e.g., gradient descent, adjoint-based methods, genetic algorithms, Bayesian optimization, etc.) each featuring its pros and cons. BO has been a well-established method within the machine learning community as optimization tool for over a decade. In fact, although the initial intuition behind the philosophy of Bayesian optimization can be traced back to Ref. [54], it was not until 1990 that the modern formulation of Bayesian optimization, with the usage of the Gaussian process regression, was introduced [55]. Pioneering applications of BO in fluid dynamics are those reported in Refs. [56,57,41].

The Bayesian optimization framework comprises two main components: a probabilistic surrogate model and an acquisition policy. The surrogate model encapsulates our beliefs about the function's behavior and is continually updated with the newly acquired data, potentially corrupted by noise (e.g., incomplete convergence of the CFD simulation or finite time averaging in unsteady flows). The acquisition policy, however, determines the next sampling point based on a combination between the observed data and the selected strategies which usually trades exploration and exploitation. The analytical description of the BO formulation is reported in Appendix B.

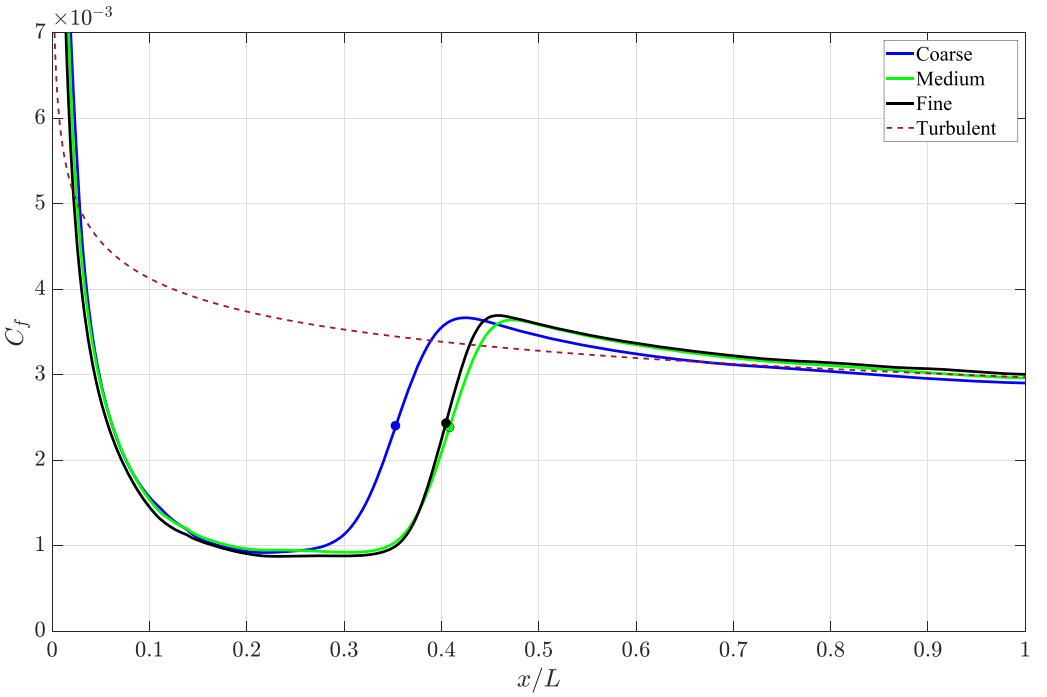

FIG. 2. Grid effect on the friction coefficient ($C_f(x/L)$), showing: (- -) the empirical law for a turbulent flat plate and (•) the estimated transition locations (x_t/L).

An optimization problem can be expressed as follows:

$$\begin{aligned} &\min_{\boldsymbol{x}\in\Omega}(-f(\boldsymbol{x})),\\ &\boldsymbol{h}(\boldsymbol{x}) \leqslant \boldsymbol{0}, \end{aligned} \tag{18}$$

where $\boldsymbol{h}(\boldsymbol{x})$ is the vector of the linear/nonlinear constraints.

Depending on the problem being addressed, the function $f(\boldsymbol{x})$ can be stated in two different ways:

$$f(\boldsymbol{x}) = \frac{D^N - D^{\mathrm{LFC}}}{D^N} = \mathrm{DR}(\boldsymbol{x}), \tag{19}$$

or

$$f(\boldsymbol{x}) = \frac{c_d^N - c_d^{\mathrm{LFC}}}{c_d^N} = \mathrm{PR}(\boldsymbol{x}), \tag{20}$$

where D represents the drag, while c_d denotes the power coefficient, which is introduced in Eq. (39) and explained in detail in the following subsection. The superscript N in both previous equations denotes the quantity evaluated in natural scenarios (i.e., imposing a zero suction velocity: $v_w = 0$).

In this context, $\boldsymbol{x}$ represents the vector that comprehensively outlines the suction configuration, including details about the starting position of suction x_s, the endpoint of suction x_e, and the suction velocity v_w:

$$\boldsymbol{x} = [x_s/L,\, x_e/L,\, v_w/U_\infty]. \tag{21}$$

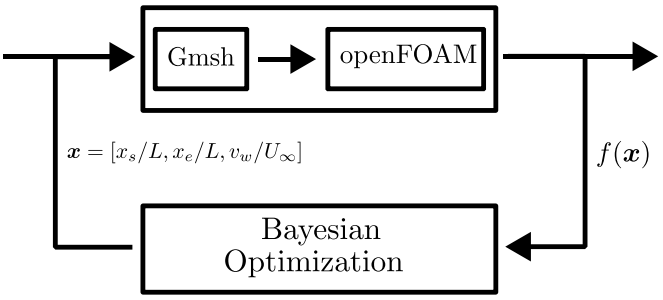

FIG. 3. Logical scheme of the LFC optimization framework considered in this study: the upper box embeds the CFD solvers, the lower one the optimization tool, while the optimization objective [$f(\mathbf{x})$] and the control parameters (x_s, x_e, v_w) are also reported.

$\Omega \subseteq \mathbb{R}^3$ defines the region of the design space in which the solution is sought, with its bounds determined by physical considerations [see Eq. (22)]. For instance, suction must begin before the point of natural transition ($\max(x_s/L) \approx 0.4558$). In addition, some clearance should be left before the trailing edges of the flat plate ($\max(x_e/L) \approx 0.8519$), while suction should start slightly downstream of the leading edge ($\min(x_s/L) \approx 0.1358$). As the threshold for the maximum absolute suction velocity, we adopt the value reported in Ref. [9], namely $v_w/U_\infty = -0.01$, which serves as the lower bound.

$$\begin{aligned}\Omega &= [[\min(x_s/L), \max(x_s/L)],\ [\min(x_e/L), \max(x_e/L)],\ [\min(v_w/U_\infty), \max(v_w/U_\infty)] \\ &= [[0.1358,\ 0.4558],\ [0.1358,\ 0.8519],\ [-0.01,\ 0]].\end{aligned} \tag{22}$$

The linear and nonlinear constraints are associated with both the relative positions of x_s and x_e—which define the width of the suction region—and the maximum permissible mass flow rate. Specifically, the width of the suction region is constrained to a minimum of 1.3% and a maximum of 50% of the total length. The upper limit for the allowable mass flow rate is 0.01 [m^3/s].

To conduct the optimization, we utilized the `bayesopt` function from MATLAB Statistics and Machine Learning Toolbox [58]. Figure 3 illustrates the relationship among the three key participants in the optimization process. The Bayesian optimization routine in MATLAB takes the objective function value from the computational fluid dynamics (CFD) solver (OpenFOAM) as input and determines the new evaluation point. The geometry and mesh corresponding to this new set of design parameters are then generated using Gmsh, which produces the updated geometry and mesh for OpenFOAM (these steps are described in detail in the next section). With the new geometry and boundary conditions set by the Bayesian optimizer, OpenFOAM simulates the flow field and, subsequently, returns the objective function value to the function `bayesopt`.

D. Power budget analysis

The preponderance of historical literature on LFC has been predominantly concerned with the delay of transition induced by LFC technologies. However, it is crucial to acknowledge that postponing transition does not invariably correlate with reductions in total drag or enhancements in energy efficiency. Therefore, this study primarily focuses on evaluating energy usage, with secondary considerations of drag and transition serving to emphasize the importance of energy management. In this analysis, a suction configuration is deemed viable if it results in a reduction in power consumption compared to the baseline scenario—the power required in the natural, uncontrolled state.

The total power can be dissected into the power necessary to overcome drag—essential for propelling the flat plate at a uniform speed—and the power expended by the pump to feed the suction mechanism.

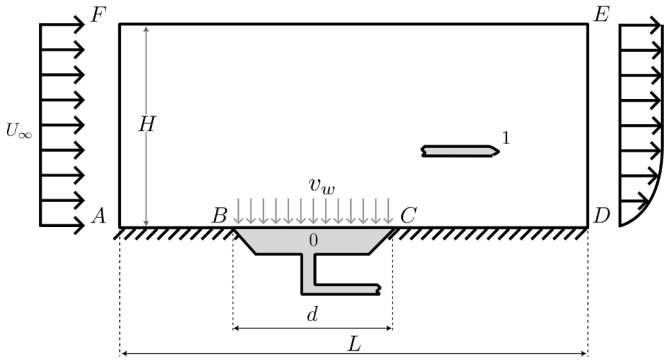

FIG. 4. Schematic (not-to-scale) of the fluid domain showing the wall-suction system (in gray) and some relevant quantities: free-stream velocity (U_∞), suction velocity (v_w), suction slot width (d), domain height (H) and length (L), suction system inlet (0) and outlet (1), somewhere in the fluid domain.

Discussing drag necessitates precision, particularly when wall transpiration is a factor. Prior studies [1,38–40] have delineated the distinction between wake drag and body drag, which difference is to be addressed to the volume of air transferred from the boundary layer to the suction system. This relationship between wake drag, body drag, and mass flow involved in LFC can be clarified through a simple momentum analysis of a control volume that encapsulates the aerodynamic model (i.e., the plate in this study).

Considering the LFC system depicted in Fig. 1, and assuming uniform velocities for both the free stream and the suction, the continuity equation can be formulated as follows:

$$HU_\infty - dv_c - \int_{DE} u(y)\,dy = 0, \tag{23}$$

where H is the height of the domain and d the width of the suction region (see the LFC domain schematics of Fig. 4). Furthermore, if we assume uniform pressure throughout the domain and hypothesize that the flow is, at least statistically, in a steady state, it follows that the momentum within the control volume remains constant over time. Applying the momentum balance under these assumptions enables us to establish an additional relationship between the quantities involved in the previous equation. Indeed, the momentum balance reads

$$\underbrace{\int_{AD} \boldsymbol{\tau_w} \cdot \boldsymbol{n}\,d\sigma}_{-\boldsymbol{F}} = \int_{\partial\Omega} \boldsymbol{U}(\boldsymbol{U}\cdot\boldsymbol{n})\,d\sigma, \tag{24}$$

with $\boldsymbol{F}$ the force that the fluid exerts on the plate. Projecting $\boldsymbol{F}$ into the U_∞ direction leads to the body drag D:

$$D = \int_{AD} \tau_w\,dx = \rho\left(\int_{DE} U_\infty^2 - u^2(L,y)\,dy\right). \tag{25}$$

Finally, substituting Eq. (23) into Eq. (25), we derive

$$\underbrace{D}_{\text{Body Drag}} = \underbrace{\rho\,U_\infty^2 \int_{DE} \frac{u(L,\,y)}{U_\infty}\left(1 - \frac{u(L,\,y)}{U_\infty}\right)dy}_{\text{Wake Drag}} + \underbrace{\rho\,v_w\,dU_\infty}_{\text{LFC Drag}}. \tag{26}$$

As stated by Beck *et al.* [1], in LFC scenarios, only the body drag provides a true measure of the effort required for a plate to advance through the air at a relative velocity equal to U_∞. By multiplying the body drag by the free-stream velocity, we obtain the external power needed—

typically provided by the engine thrust—to sustain the plate's constant velocity at U_∞. Completing the momentum analysis requires determining the fate of the ingested air. There are two options: storing it onboard or expelling it. Storing the air in a tank, especially in an aircraft, introduces a significant weight penalty, making it impractical. Consequently, the only viable option is to expel the ingested air. This expelled air can be used further for flow control that requires blowing or to simply generate thrust. In this study, which focuses solely on suction, we opt for the latter approach. Expelling the air at a velocity U_{jet} produces a small amount of additional thrust $T = \dot{m}\, U_{\text{jet}}$, which effectively helps to alleviate the drag. Associated with this thrust, there is the power term: TU_{jet}.

The question regarding the power required to operate the pump that actuates the suction is predominantly addressed by evaluating the difference in enthalpy between the flow entering and exiting the suction system. In the sketch in Fig. 4, the control volume associated with the suction system is highlighted in gray. The subscript "0" denotes the inlet to the suction system control volume, and "1" marks the outlet, somewhere in the fluid domain. Under the boundary layer assumption, the pressure and velocity at the inlet of the suction control volume are equal to the free-stream static pressure and the suction velocity, respectively. Therefore, the BCs at the domain inlet are

$$U_0 = \lim_{y\to 0^+} ||\boldsymbol{U}(\boldsymbol{y})|| = v_w, \quad P_0 = \lim_{y\to 0^+} P(y) = P_\infty. \tag{27}$$

Assuming an adiabatic evolution of the flow from the entry point 0 to the exit point 1, the energy required by the flow can be expressed by the following equation:

$$W = \dot{m}\left[\frac{1}{2}\left(U_1^2 - U_0^2\right) + \frac{P_1 - P_0}{\rho}\right] + L^{\text{tot}}, \tag{28}$$

where L^{tot} represents the total losses related to friction and changes in the cross-sectional area of the suction system. These losses can be further decomposed into the sum of the losses the fluid experiences within the distribution systems L^{fric} (i.e., the pipes that carry the fluid from point "0" to point "1") and the losses L^{por}associated with the passage through the porous material. Estimating these losses is challenging, as they depend significantly on the specific design choices made. Fahland *et al.* [39] addressed this issue by assuming that the maximum pressure loss coefficient within the air distribution system (Δc_p^{fric}) was equal to 0.1. To align with established literature, this study also adopts this assumption for the distribution system, but it differs from the literature itself by imposing a different dependency of L^{fric} with respect to v_w. L^{fric} [Eq. (31)] can be expressed by the product between the volumetric mass flow $\dot{q}$ [Eq. (29)] and the pressure losses Δp^{fric} [Eq. (30)] in the circuit. The former depends linearly on the suction velocity, while the latter quadratically:

$$\dot{q} = v_w d = \frac{\dot{m}}{\rho}, \tag{29}$$

$$\Delta p^{\text{fric}} = \Delta c_p^{\text{fric}} \tfrac{1}{2}\rho v_w^2, \tag{30}$$

$$L^{\text{fric}} = \dot{q}\Delta p^{\text{fric}} = \tfrac{1}{2}\rho v_w^3 d\, \Delta c_p^{\text{fric}}. \tag{31}$$

It is important to highlight the difference between the formulation presented here and the one proposed in Ref. [39]. While Eq. (31) results in a cubic function of v_w, the formulation by Fahland *et al.* [39] shows a linear dependency on this velocity.

The modeling of pressure losses through the porous wall is governed by Forchheimer's equation [59], which is expressed as

$$\frac{\Delta p}{t_{\text{pp}}} = \frac{\mu}{k_1} v_w + \frac{\rho}{k_2} v_w^2, \tag{32}$$

where Δp represents the pressure drop across the porous wall, t_{pp} the porous panel's thickness, while k_1 and k_2 are the Darcian and non Darcian permeability coefficients, respectively. Compared with the more common and simpler Darcy law, in which only the linear term is consider, the Forchheimer's

equation offers more reliable correlations especially for a large range of suction velocities, where both small and high velocity are encompassed [60]. Given the Darcian permeability, the non-Darcian coefficient k_2 can be estimated using a robust empirical correlation:

$$k_2 = \exp\left(-1.71588\, k_1^{-0.08093}\right). \tag{33}$$

Expressing again the power as the product between the pressure drop and the volumetric mass flow:

$$L^{\text{por}} = \dot{q}\Delta p = dt\, v_w^2\left(\frac{\mu}{k_1} + \frac{\rho}{k_2} v_w\right). \tag{34}$$

Assuming the pressure at which the air is discharged is equal to $p_\infty (P_0 = P_1 = p_\infty)$ and also recalling that $U_1 \equiv U_{\text{jet}}$ and $U_0 \equiv v_w$, the power required to change the fluid's pressure and velocity from condition 0 to condition 1 is given by

$$W = \dot{m}\left[\frac{1}{2}\left(U_1^2 - v_w^2\right) + \frac{1}{2} v_w^2 \Delta c_p^{\text{loss}} + \frac{t v_w}{\rho}\left(\frac{\mu}{k_1} + \frac{\rho}{k_2} v_w\right)\right]. \tag{35}$$

Considering that every turbomachine has its own efficiency (η_{pump}) in converting power, the external power we must provide to the pump is

$$W^{\text{pump}} = \frac{W}{\eta_{\text{pump}}} = \frac{\dot{m}}{\eta_{\text{pump}}}\left[\frac{1}{2}\left(U_{\text{jet}}^2 - v_w^2\right) + \frac{1}{2} v_w^2 \Delta c_p^{\text{loss}} + \frac{t v_w}{\rho}\left(\frac{\mu}{k_1} + \frac{\rho}{k_2} v_w\right)\right]. \tag{36}$$

Finally, by adding the power from the momentum analysis and the power from the pump, we can express the total power as

$$W^{\text{total}} = \frac{(D - \dot{m} U_{\text{jet}}) U_\infty}{\eta_{\text{prop}}} + \frac{\dot{m}}{\eta_{\text{pump}}}\left[\frac{1}{2}\left(U_{\text{jet}}^2 - v_w^2\right) + \frac{1}{2} v_w^2 \Delta c_p^{\text{loss}} + \frac{t v_w}{\rho}\left(\frac{\mu}{k_1} + \frac{\rho}{k_2} v_w\right)\right], \tag{37}$$

where η_{prop} is the overall engine efficiency, usually represented as the product between the thermal and the propulsive efficiency. The remaining challenge is to determine the optimal value of U_{jet}. The most advantageous expelled air velocity is the one that minimizes the total power W^{total}, which requires satisfying the condition $\partial W^{\text{total}}/\partial U_{\text{jet}} = 0$. From this relation, the optimal jet velocity is obtained as

$$U_{\text{jet}} = \frac{\eta_{\text{pump}}}{\eta_{\text{prop}}} U_\infty. \tag{38}$$

Following the lead of Refs. [1,38,41], in this work, particular emphasis will be given to the power coefficient, which is calculated by nondimensionalizing the power relative to the free-stream dynamic power:

$$\begin{aligned} c_d^{\text{LFC}} &= \frac{W^{\text{total}}}{\frac{1}{2}\rho U_\infty^3 L} \\ &= \underbrace{\frac{c_d}{\eta_{\text{prop}}}}_{c_d^I} \underbrace{- \frac{d}{L}\frac{\eta_{\text{pump}}}{\eta_{\text{prop}}^2} c_q - \frac{1}{\eta_{\text{pump}}}\frac{d}{L} c_q^3}_{c_d^{II}} + \underbrace{\frac{d}{L}\frac{\Delta c_p^{\text{loss}}}{\eta_{\text{pump}}} c_q^3 + \frac{2}{\eta_{\text{pump}}}\frac{t d}{\rho L} c_q^2\left(\frac{\mu}{k_1 U_\infty} + \frac{\rho}{k_2} c_q\right)}_{c_d^{III}}. \end{aligned} \tag{39}$$

Given that, for $c_q = v_w/U_\infty = 0$, the power coefficient simplifies to the classical drag coefficient, the interpretation of c_d^{LFC} becomes straightforward. Indeed, it can be considered as the equivalent drag coefficient in LFC scenarios where the additional power is converted into equivalent drag. This interpretation allows for a direct comparison of LFC effectiveness against traditional drag measures.

Upon examining Eq. (39), it may appear trivial, but it is worth noting that the power coefficient depends both explicitly and implicitly on the dimensionless parameters c_q and d/L (since c_d varies with the suction configuration). The components of c_d^{LFC} can be categorized into three distinct groups. The second group, indicated by c_d^{II} in Eq. (39), aids in reducing the power coefficient for

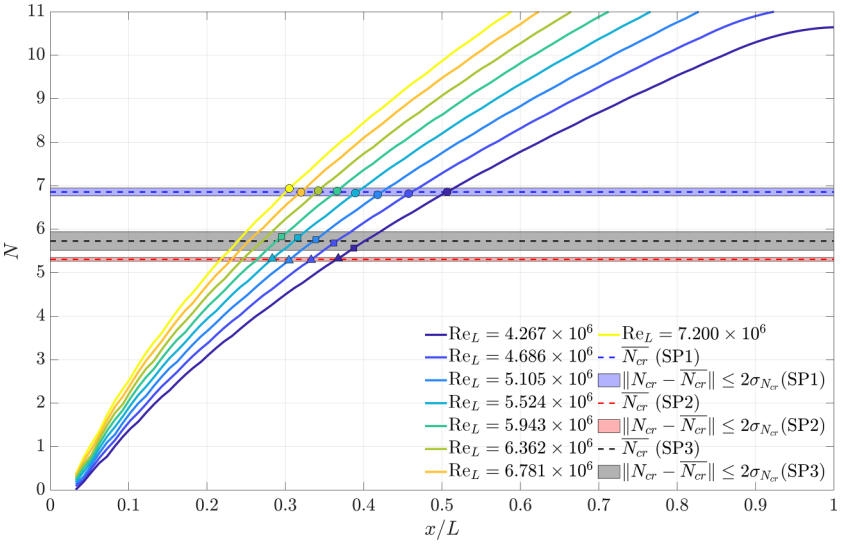

FIG. 5. N factors streamwise evolution and transition locations (x_t/L), for different Re_L, measured by Corelli Grappadelli *et al.* [9] and for the (•) SP1, (■) SP2, and (▲) SP3 panel. The dashed lines represent the average $\overline{N_{\mathrm{cr}}} = \overline{N(x_t/L)}$ for each suction panel, while half width of the filled regions corresponds to the transition predictions' standard deviation ($\sigma_{N_{\mathrm{cr}}}$).

any suction configuration, thereby enhancing efficiency. Conversely, the third group, represented by c_d^{III}, tends to increase the power coefficient, thus penalizing efficiency. However, the most critical role is played by the drag coefficient c_d^I, in Eq. (39), as it directly takes in account the overall friction drag. Large changes in the value of c_d will be reflected in large changes in the value of c_d^{LFC} as well.

III. RESULTS

A. Natural transition

In this section, the linear stability theory predictions of the natural transition location are first compared with the results obtained from CFD simulations employing the γ-Re_θ transition model. This initial validation serves a dual purpose: it confirms the robustness of the computational framework used in the simulations and provides a reference point for assessing the accuracy of the employed methods. This comparison is particularly important when analyzing LFC cases, where a reduction in prediction accuracy is expected due to the increased complexity introduced by active control mechanisms.

The laminar velocity profiles, for which stability was calculated, were determined through the integration of the Blasius equations. Employing linear stability theory and the e^N method, as briefly described in Sec. II, the N factors were computed for a theoretical flat plate subjected to a variable free-stream velocity, corresponding to a Reynolds number Re_L ranging from 4.2667×10^6 to 7.2000×10^6. The effect of increasing the Reynolds number is immediately evident from Fig. 5, resulting in more rapid disturbances' growth as the velocity increases, thereby leading to the transition promotion. The critical N factors can be derived from experimental data that correlates the transition location x_t and Re_L. These are shown in Fig. 5 for all the three panels considered in Ref. [9]. Specifically, the SP1 panel refers to the solid panel, while the SP2 and SP3 panels are porous, with 1% porosity and average holes diameters of 120 μm and 240 μm, respectively. Figure 5 clearly shows that N_{cr} is relatively constant and independent from the free-stream velocity for a given panel.

TABLE VI. Statistics about the e^N method predictions for different suction panels (SP). The first column indicates the mean value of N_{cr}, the second its standard deviation, while the last is a measure of the method accuracy.

SP	$\overline{N_{cr}}$	$\sigma_{N_{cr}}$	$2\sigma_{N_{cr}}/\overline{N_{cr}}$ [%]
SP1	6.86	0.04	1.3
SP2	5.31	0.11	3.7
SP3	5.73	0.02	0.8

Notably, the largest N_{cr} value observed pertains to the full panel SP1, demonstrating that the mere introduction of a porous wall (panels SP2 and SP3) has an inherently destabilizing effect. This destabilizing effect is attributed to the introduction of small disturbances in the wall normal velocity component through the micro orifices of the porous panel [61].

For each panel, a statistical analysis of the different measured N_{cr} was conducted, focusing particularly on the mean value and standard deviation, as reported in Table VI. Figure 5 illustrates that all the measured critical N factors fall within an interval of $\pm 2\,\sigma_{N_{cr}}$ from the mean value. Consequently, considering $\pm 2\,\sigma_{N_{cr}}$ as a measure of the method's accuracy, the uncertainty in the N_{cr} for natural transition is ± 1.3 % and ± 0.8 % for panels SP1 and SP3, respectively. For panel SP2, the uncertainty is higher and is attributed to the N_{cr} associated with $\mathrm{Re}_L = 4.2667 \times 10^6$, which differs significantly from the others, thus increasing the overall uncertainty.

It is interesting to note the comparison between the critical N value from Figs. 5 and 16 in Ref. [9]. The N_{cr}, computed based on our N envelopes are more clustered around the mean than the ones found by Corelli Grappadelli *et al.* [9]. This discrepancy, assumed to be related to the differing grid resolutions used in the computation of the N envelope, prompted us to reevaluate the N_{cr} results reported in Ref. [9] for the LFC case (see Sec. III B), employing a finer grid resolution than what Fig. 17 from Ref. [9] suggests was adopted.

Given the main goal of any active flow control-drag reduction oriented technique is to reduce the power and the drag, employing the γ-Re_θ model has the advantage to directly retrieve the integral friction drag, which is related to the the area underneath the curves in Fig. 6. The transition location x_t/L is defined as the inflection point of the friction coefficient. The challenges in modeling the destabilizing effect of the porous media of the suction panels led us to study only the solid panel SP1. The impact of increasing the Reynolds number becomes evident as the transition location shifts upstream (see Fig. 6). The model's accuracy in predicting the transition is excellent at low velocities. Specifically, for $\mathrm{Re}_L < 5.3333 \times 10^6$, there is a strong agreement between experimental results, numerical simulations, and LST (see Fig. 7). However, for Reynolds numbers exceeding 5.3333×10^6, the predictions of the γ-Re_θ model diverge from the experimental observations, although they still remain within the uncertainty reported in Ref. [9].

B. LFC

Extensive simulations have been conducted to predict the streamwise displacement of the transition point x_t/L when steady and uniform suction control is employed. These predictions are, once again, compared to the experimental data from Ref. [9]. The experimental tests, focused on the impact of suction on a flat plate BL flow, were carried out at five different Reynolds numbers. For each Re_L, a relationship between the suction intensity c_q and the transition abscissa is represented by a curve. This curve provides a relation between c_q and x_t/L for every c_q within the range explored in the experiments, allowing us to perform the validation tests for any arbitrary value of suction velocities. Through this thorough testing, more confident conclusions can be drawn.

Using the LST on the boundary layer subject to active control and leveraging the experimental curves, an assessment of the accuracy and applicability of the e^N transition criterion is conducted. To achieve this, the velocity profiles, which are used as inputs for the LST solver, are derived by

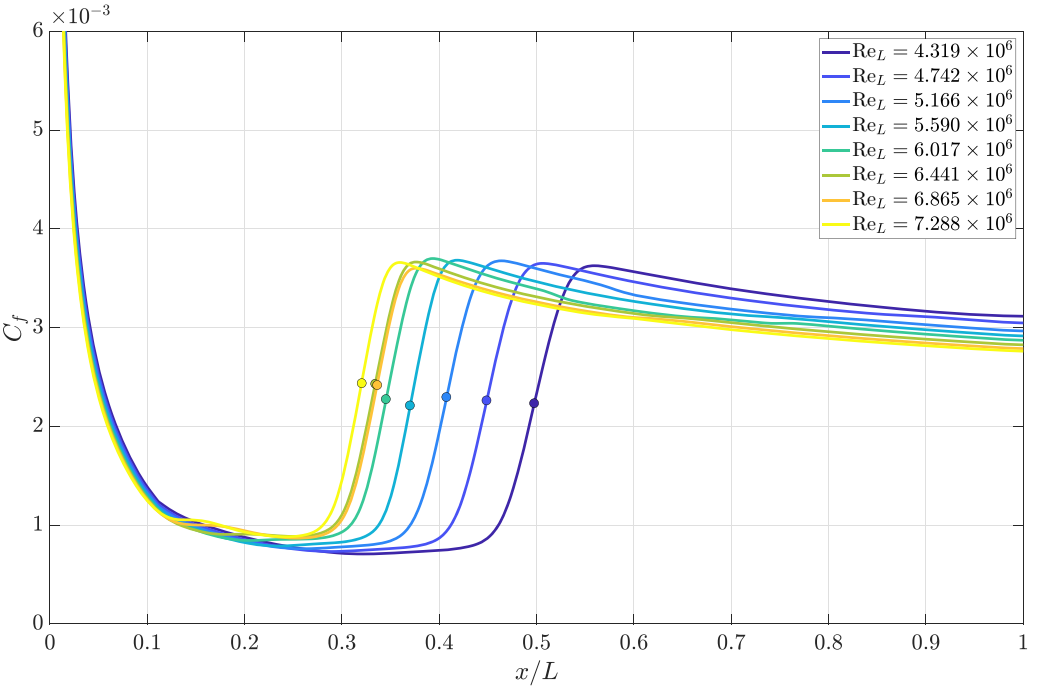

FIG. 6. (—) Streamwise evolution of skin friction coefficients (C_f) and (•) transition locations (x_t/L) predicted by the γ-Re_θ model, for different Re_L.

solving the boundary layer equations with the appropriate boundary conditions, specifically with $v_w \neq 0$ inside the suction region. The results of this analysis are illustrated in Fig. 8. The stabilizing effect of suction is evident by the slower growth or even reduction of the N factors inside the suction region. While the range through which the critical N factors span is different from the one explored in Ref. [9], the same qualitative behavior is observed. Specifically, for small values of the suction coefficient c_q, a steady decrease in N_{cr} is observed, indicating that the boundary layer is less stable compared to the LST prediction (Fig. 8). The minimum N_{cr} is approximately 1.7 times lower than the natural critical value [Fig. 8(b)]. If a constant N_{cr} had been assumed, the predicted transition point would have been approximately 7 % of the plate length downstream, compared to the actual transition location. After reaching the minimum value of N_{cr}, the trend reverses, and an increase in the suction coefficient leads to an increase in N_{cr}. Corelli Grappadelli *et al.* [9] attributed this behavior to the nonlinear/nonparallel phenomena that LST is unable to capture, or in other words, LST is unable to model the stability of the boundary layer subject to suction.

Although the hypothesis proposed in Ref. [9] is plausible, it is unlikely to be the sole contributing factor. Two additional mechanisms may account for the observed variability of N_{cr} during suction. The first pertains to disturbances introduced by the suction system—originating from the pump and transmitted through the porous wall—into the boundary layer. The absence of a sonic nozzle, as employed in Ref. [7] to prevent upstream propagation of disturbances through the suction conduits, may partially explain the nonconstancy of N_{cr}. It is hypothesized that these disturbances are particularly influential at low mass flow rates but diminish as the flow rate approaches the design regime. At sufficiently high suction velocities the value of N_{cr} tends to converge toward 7, which corresponds to the critical N factor associated with the nonperforated panel SP1. When c_q exceeds a certain threshold ($\simeq 2 \times 10^{-4}$), both the disturbances induced by transpiration through the porous surface and those introduced by the suction pump become negligible, thereby restoring

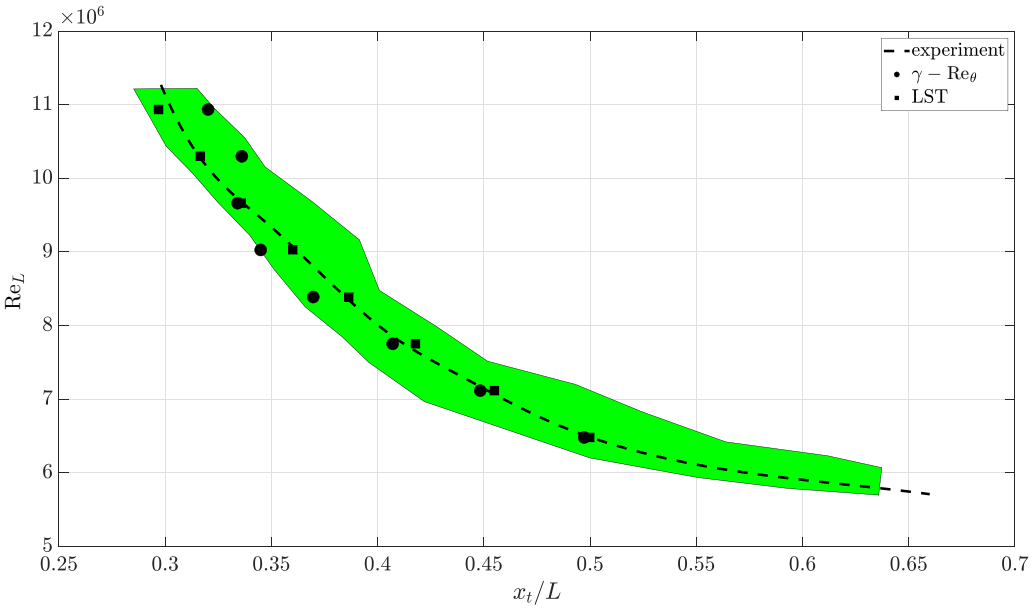

FIG. 7. Normalized natural transition location (x_t/L) for different Re_L showing: (- -) data from Ref. [9] (panel SP1), (■) x_t/L predicted by LST + e^N, and (•) by the γ-Re_θ model. The green shaded region denotes the experimental uncertainty for the transition location (see Ref. [9]).

the dominance of free-stream perturbations in the transition process. A second contributing factor to the variability of N_{cr} may be the occurrence of over-suction effects [10,33–35].

In light of the limited accuracy of the γ-Re_θ transition model at high Reynolds numbers ($\geqslant 5.3333 \times 10^6$), we chose to compare the simulated and experimental $c_q - x_t/L$ curves within this velocity limit. This led us to select the $c_q - x_t/L$ curve corresponding to $\mathrm{Re}_L = 5.1300 \times 10^6$. Another challenge we faced was addressing the destabilizing effect of the porous medium, which cannot be accurately modeled. Since the transition point is further downstream in the case of natural transition on a solid panel compared to when using a porous medium, we decided to conduct numerical simulations while maintaining the same relative distance between the suction region and the natural transition point. Therefore, in the simulations, the suction region was rigidly translated downstream of $0.0988\,L$ (0.4 m).

In the low suction regime, the γ-Re_θ model demonstrates superior performance compared to the e^N method, as shown in Fig. 9. Specifically, the transitional turbulence model accurately captures two critical characteristics identified by Corelli Grappadelli *et al.* [9]. Firstly, it effectively represents the slope of the quasi-linear segment, which is a Re_L, dependent parameters [9]. For $c_q < 2.5 \times 10^{-4}$, the CFD-computed transition displacement closely aligns with the experimental curve. The second important feature is the knee of the "exponential" curve as described in Ref. [9]. The knee represents the region where the c_q-x_t/L curve bends over, indicating a change in the response of the boundary layer to the downstream transition shifting due to suction. Although qualitative CFD and experimental data agree, there are significant quantitative differences, especially in the interval $3.0 \times 10^{-4} \leqslant c_q \leqslant 1.1 \times 10^{-3}$. The CFD model error in this range goes from 3% to 6% of the plate's total length, resulting in a discrepancy between the experimental transition point from $0.0296\,L$ to $0.0596\,L$ (0.12 m to 0.24 m). The friction coefficient distribution for each numerically tested suction coefficient is depicted in Fig. 10. In Fig. 11 a linear relation between the DR and the suction coefficients can be found, at least for small suction values. Local increases in the friction coefficient are observed in the region where suction is applied. However, this increase is compensated by the downstream shifting of the transition point. The combination of these two

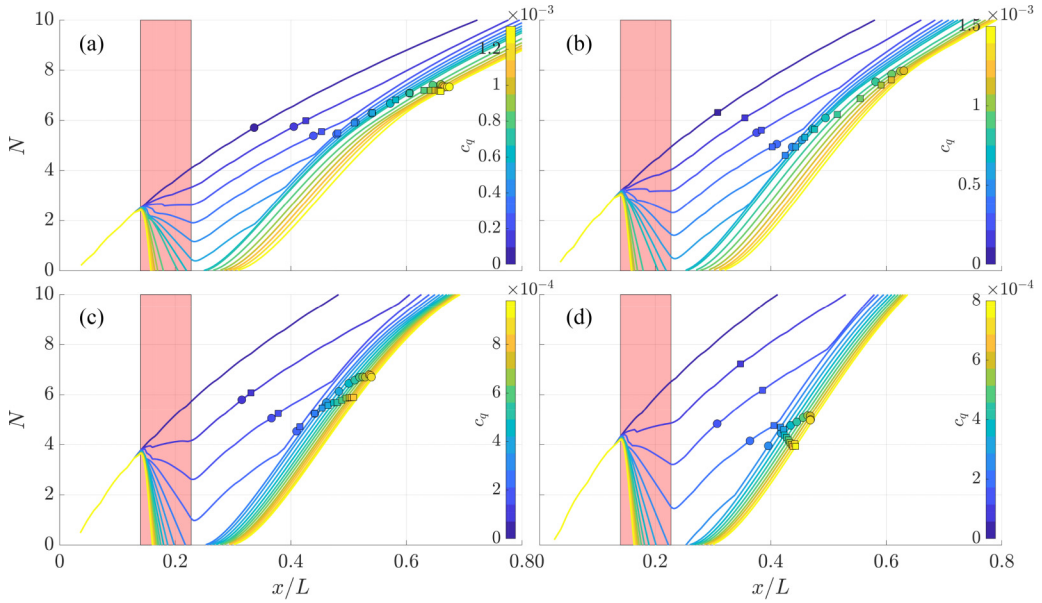

FIG. 8. Streamwise evolution of N factors color coded with c_q. Are also shown: (red shade) the LFC region and the experimental transition points for: (■) SP2 and (●) SP3; panels (a)–(d) pertain to $\mathrm{Re}_L = [5.1300,\ 6.3990,\ 7.6950,\ 9.0450] \times 10^6$, respectively.

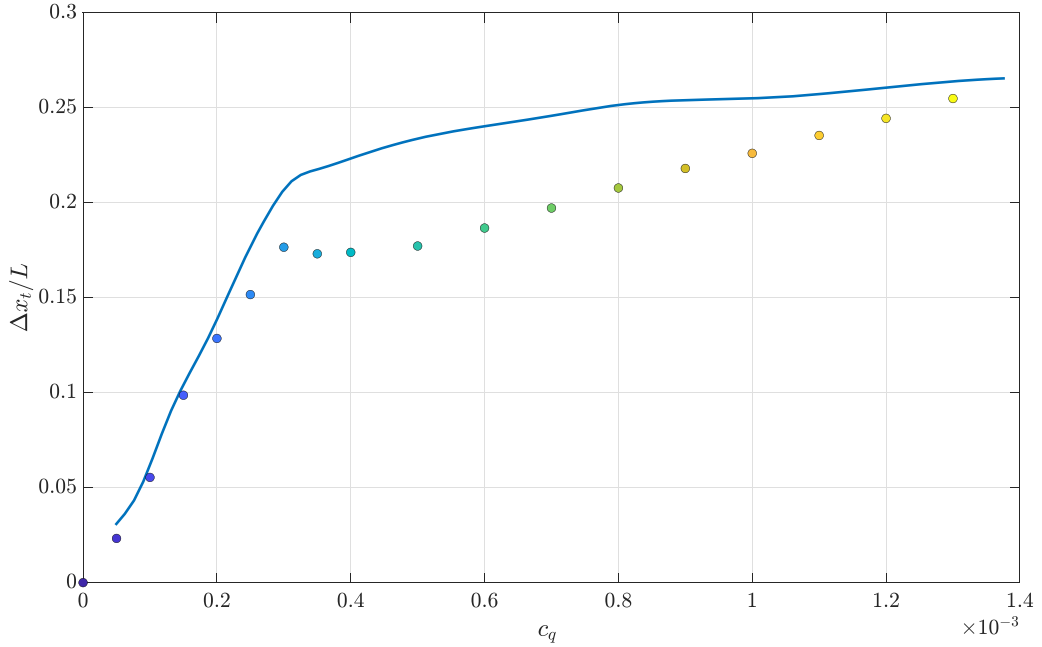

FIG. 9. Normalized transition displacement ($\Delta x_t/L$) for different values of the suction coefficient (c_q): (—) experimental data from Ref. [9] and (●) CFD predictions.

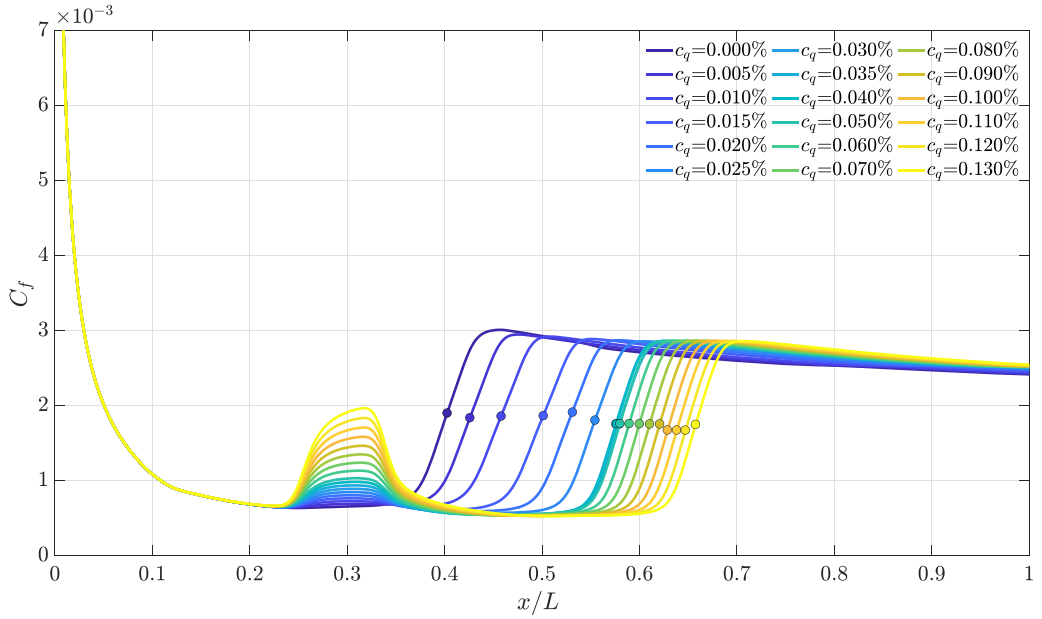

FIG. 10. (—) Streamwise evolution of the friction coefficient (C_f) and (•) estimated transition locations (x_t/L), for different values of the suction coefficient (c_q).

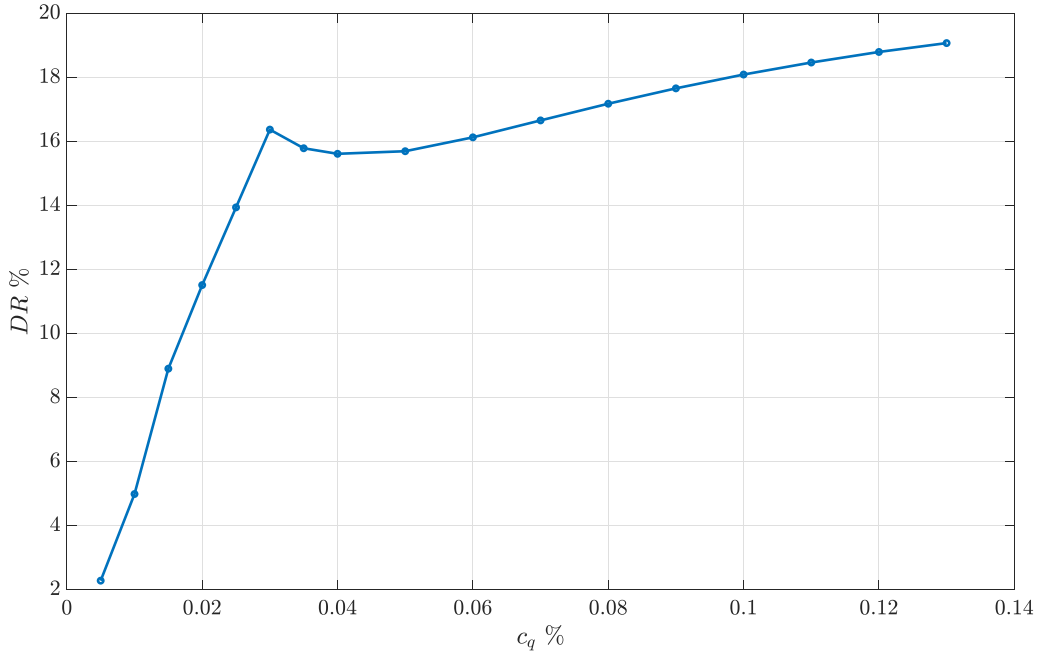

FIG. 11. Estimated CFD drag reduction (DR), defined by Eq. (40), for different values of the suction coefficient (c_q).

effects leads to an overall reduction in the area underneath the Cf curve, indicating an overall reduction in friction drag.

In particular, the DR is defined as follows:

$$\mathrm{DR}\,[\%] = \frac{D_f^N - D_f^S}{D_f^N} \times 100, \tag{40}$$

where D_f^N is the friction drag in case of natural transition and D_f^S represents the friction drag resulting from suction control.

A linear relation between the DR and the suction coefficients can be found, at least for small suction values. For c_q values comprised in the range $3 \times 10^{-4} \leqslant c_q \leqslant 1.1 \times 10^{-3}$, the underestimation of the transition shifting results in an underestimation of the DR parameter. When c_q approaches the value close to 1.5×10^{-3}, the CFD computed transition points tend to match again the experimental value (see Fig. 9), suggesting that also the friction drag will be closer to the real one. Although the drag reduction experienced for this value of the suction parameter is higher than the drag reduction achievable in the linear region, the efficiency in the DR capabilities is notably decreased, since quadrupling the value of c_q results in only an addition 3 % of reduced drag.

IV. DISCUSSION

To contextualize the ensuing discussion on the optimization of power reduction, it is proper to outline the parameter settings first. The optimization loop considers a porous panel characterized by a thickness $t = 4\,\mathrm{mm}$, likely made by a laser-perforated titanium plate [40]. The Darcian permeability coefficient is set at $k_1 = 1.00 \times 10^{-12}\ \mathrm{m}^2$ [62], and the non-Darcian coefficient, derived using the Eq. (33), is $k_2 = 1.06 \times 10^{-7}\,\mathrm{m}$. The pump efficiency is fixed at $\eta_{\mathrm{pump}} = 0.7$ (see, e.g., Refs. [1,42]), whereas, the propulsive efficiency is assumed to be $\eta_{\mathrm{prop}} = 1$.

In Eq. (37), three distinct terms are identified and represented by the symbols W_1, W_2, and W_3 as illustrated in the following equation:

$$W^{\mathrm{total}} = \underbrace{\frac{DU_\infty}{\eta_{\mathrm{prop}}}}_{W_1} - \underbrace{\frac{1}{2}\frac{\dot{m}}{\eta_{\mathrm{pump}}}\left(\frac{\eta_{\mathrm{pump}}^2}{\eta_{\mathrm{prop}}^2}U_\infty^2 + v_w^2\right)}_{W_2} + \underbrace{\frac{\dot{m}}{\eta_{\mathrm{pump}}}\left[\frac{1}{2}v_w^2\Delta c_p^{\mathrm{loss}} + \frac{t v_w}{\rho}\left(\frac{\mu}{k_1} + \frac{\rho}{k_2}v_w\right)\right]}_{W_3}. \tag{41}$$

The terms W_1, W_2, and W_3 correspond, respectively, to the coefficients c_d^I, c_d^{II}, c_d^{III} as defined in Eq. (39), and they possess identical interpretations. It is to be noted that, for the natural unforced flow, the only power term left corresponds to W_1 and, being referred to the natural flow, it is named W_N in the remainder. The dependency of W_1 on the suction configuration $\boldsymbol{x}$ is complex, necessitating the use of a CFD solver for resolution. In contrast, W_2 and W_3 exhibit explicit, direct relationships with the suction configuration: they are linear functions of the mass flow rate $\dot{m}$ and polynomial functions of the suction velocity v_w as demonstrated in Fig. 12. The function $W_2/\dot{m}U_\infty^2$, which quantifies the benefits of expelling the sucked mass flow to gain thrust, remains nearly constant across a wide range of v_w. Conversely, $W_3/\dot{m}U_\infty^2$ shows a rapid increase over the same interval. The intersection of these two curves occurs at a suction coefficient $c_q \sim 4.5 \times 10^{-5}$, indicating that this is likely the optimal value for power reduction.

The power reduction optimization investigated 700 different configurations. Following the criteria outlined in Ref. [41], the conclusion of the optimization loop is governed by monitoring both the expected improvement (EI) and the maximum response value (the evolution of τ over the iterations). As the optimization advances and more information about the objective function is collected, the maximum value of the EI function is expected to decrease. This is shown in the left plot of Fig. 13. Once the function's optimum is found, further improvements in the best response value are unlikely. Therefore, convergence to the global optimum can be inferred if, over a sufficiently large number of iterations, the maximum response value stabilizes and the EI consistently exhibits low values [41].

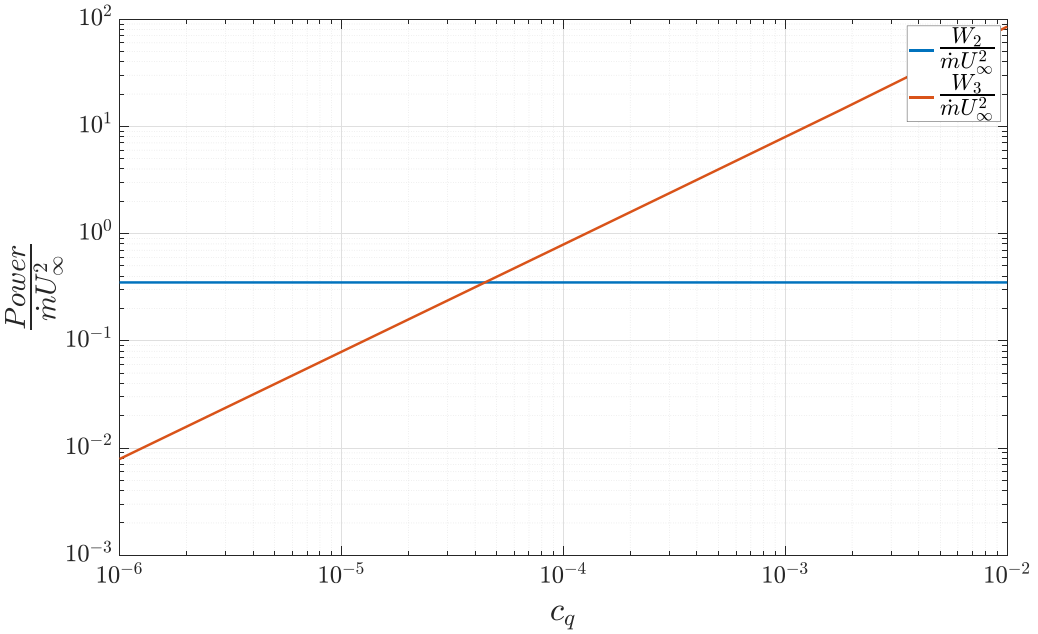

FIG. 12. Normalized W_2 and W_3 [see Eq. (41)], for different values of the suction coefficient (c_q).

The optimization performed to address the power reduction problem identified the design point $\boldsymbol{x} = [0.2437,\ 0.7254,\ -2.6395 \times 10^{-4}]$ as the optimal configuration, yielding a power reduction (PR) of 34.02 %. This outcome is depicted in the right plot of Fig. 13, which also traces the

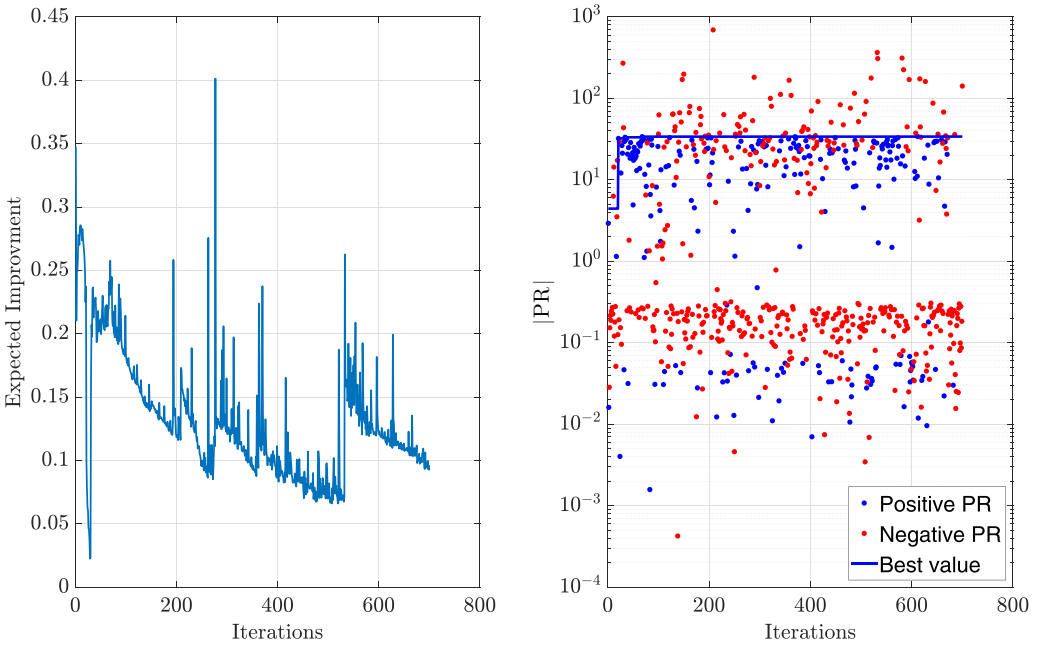

FIG. 13. (Left) Expected improvement (EI) and (right) power reduction (PR) through the iterations (with logarithmic scale for the y axis to improve visualization).

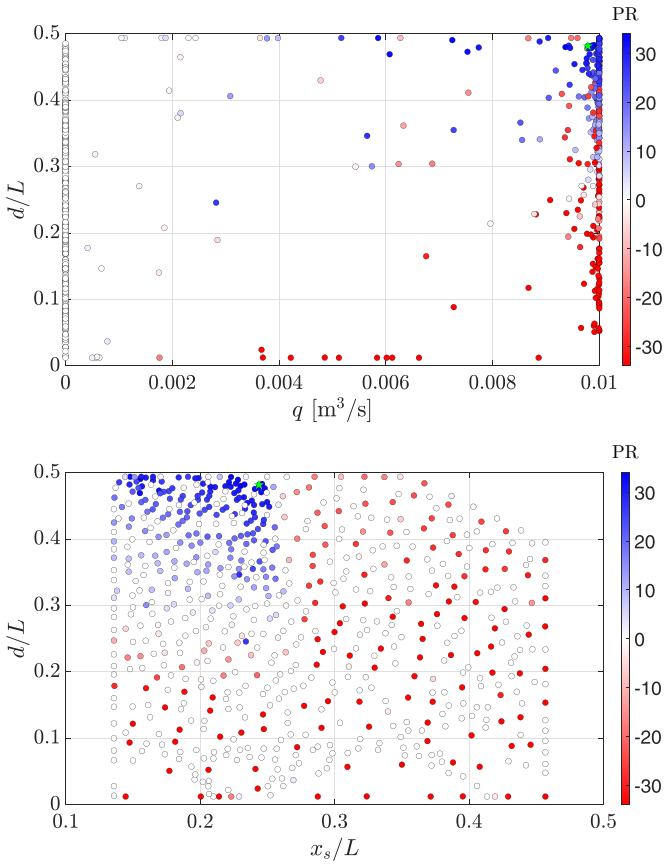

FIG. 14. PR values distribution as a function of (top) sucked mass flow rate and width of the suction region and (bottom) of the suction slot upstream location and width. The optimal configuration, for the considered optimization, is marked with a light green star in both plots. For visualization purposes, the colorbar is limited to the range [−34 %, 34 %].

progression of the best PR value throughout the optimization iterations. The achieved PR of 34.02 %, represents a substantial improvement, demonstrating the effectiveness of the proposed methodology in finding efficient LFC configurations leading to much reduced power consumption.

The optimization process generated a dataset that, upon thorough analysis, can deepen our understanding of suction as a laminar flow control technique and potentially inform the design of more effective/efficient LFC devices. Figure 14(a) shows the PR as a function of volumetric mass flow and suction region width. A twofold influence of the suction region width on PR is evident in the figure. On the one hand, the plot highlights the localized effects of suction on flow dynamics: when suction control is applied over a given region, the flow within that area tends to remain laminar. Therefore, extending the suction region leads to a larger laminar flow portion. On the other hand, for a fixed mass flow rate $\dot{m}$, decreasing d results in a higher v_w, which in turn increases the contribution of W_3 to the total drag W^{total}. Notably, W_3 grows rapidly with increasing v_w, as shown in Fig. 12. This explains the significant rise in power consumption observed when moving toward the bottom-right corner of Fig. 14.

Another variable to which the PR is highly sensitive is the location where suction control begins (x_s), as shown in Fig. 14(b). To better illustrate this point, Fig. 15 displays the skin friction coefficients for four different suction configurations: the natural transition reference case, the optimal LFC case, and two suboptimal LFC configurations that differ from the optimal one only by

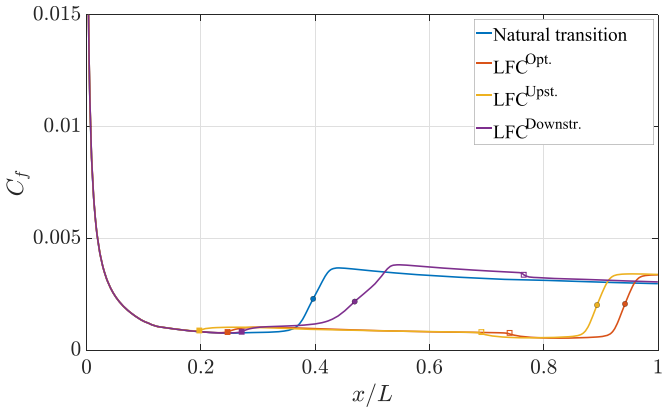

FIG. 15. (—) Streamwise evolution of the friction coefficient (C_f), for: the natural transition case, the optimal suction configuration (LFC$^{\text{Opt}}$), and the LFC$^{\text{Upst.}}$ ($\Delta x_{\text{LFC}}/L = -0.05$) and LFC$^{\text{Downstr.}}$ ($\Delta x_{\text{LFC}}/L = 0.05$) cases; also showing: (■) x_s/L, (□) x_e/L, and (•) x_t/L.

the location of the suction region. Slightly shifting the suction slot upstream ($\Delta x_{\text{LFC}}/L = -0.05$), relative to the optimal position, results in a corresponding upstream shift of the transition point, thus a modest increase in total drag due to a reduction in the laminar flow region. Conversely, postponing the initiation of suction of the same amount ($\Delta x_{\text{LFC}}/L = 0.05$) leads to more severe consequences. In this case, BL instabilities feature additional space to develop and to grow. By the time suction is activated, the perturbations have already reached such high amplitudes that the damping mechanisms introduced by suction control are no longer sufficient to attenuate them effectively, rendering the laminar–turbulent transition unavoidable.

To assess the effect that these three different LFC configurations cause, compared to the unforced reference flow, to the flow topology, we inspect the streamwise velocity component fields as well as the integral quantities that typically characterize the boundary layer, namely the BL displacement and momentum thickness. In Fig. 16, two distinct BL types can be identified: the laminar–turbulent case [Figs. 16(a) and 16(b)] and the forced-laminar case [Figs. 16(c) and 16(d)]. In the laminar-turbulent case, the classical interpretation of BL theory applies. In the laminar region, a substantial portion of the BL is occupied by low-velocity flow, which is responsible for the low velocity gradient at the wall and, consequently, a moderate friction coefficient. In the turbulent region, mixing processes characteristic of turbulence bring higher-momentum fluid closer to the wall, producing a steeper velocity gradient and a corresponding rise in wall friction (see Fig. 15). Apart from a small set of near-wall streamlines that are deflected toward the plate's surface, most streamlines are displaced away from it. This behavior is also reflected in the integral BL thickness measures. Both displacement thickness and momentum thickness increase monotonically downstream, with a noticeably higher growth rate in the turbulent region. For the forced-laminar case, the velocity field exhibits a markedly different structure. A large region of low-speed flow extends over nearly the entire plate, resulting in persistently smaller velocity gradients and related friction drag. The application of suction causes some streamlines to terminate at the wall, representing external fluid drawn into the suction system. Because the external flow is continuously entrained toward the wall by the imposed negative wall-normal velocity, both the momentum thickness and the boundary-layer thickness increase only gradually along the streamwise direction.

A visual evidence of the effect of the three hereby investigated LFC configurations on the perturbations growth is presented in Fig. 17, where the turbulent kinetic energy (TKE, k) quantifies the velocity fluctuations relative to the mean flow. In Fig. 17(a), the reference TKE field, for the natural transition case, is reported. The TKE begins to increase at approximately $x/L \simeq 0.25$ and, within a short stream distance, it reaches its maximum value, indicating the onset of turbulence. Figure 17(c) illustrates the dependence of perturbation amplitude, measured by TKE, on the optimal LFC design

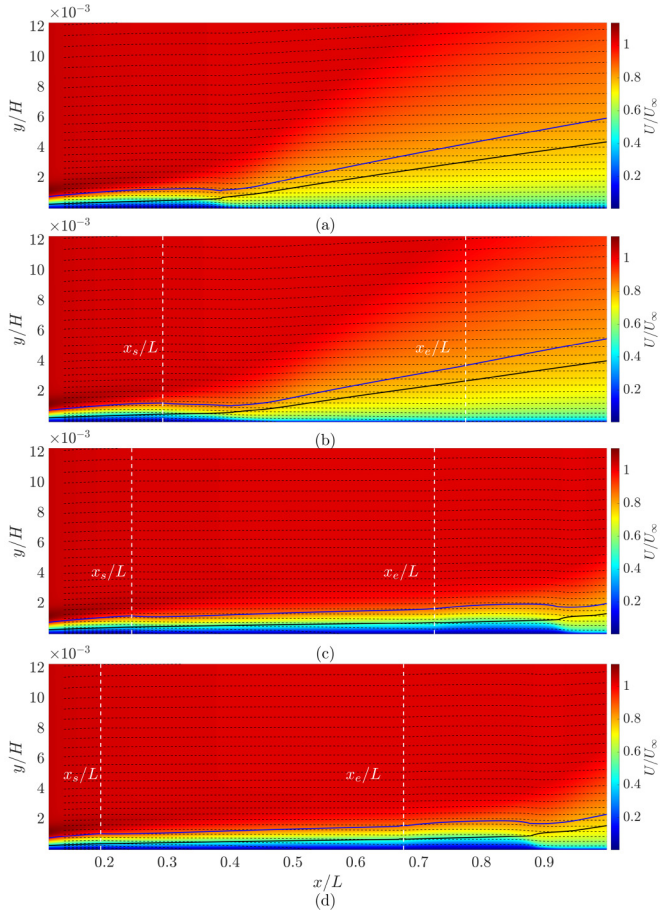

FIG. 16. Time-averaged streamwise velocity contours for: (a) the natural transition case, (b) LFC$^{\text{Downstr.}}$ ($\Delta x_{\text{LFC}}/L = 0.05$) and (d) LFC$^{\text{Upst.}}$ ($\Delta x_{\text{LFC}}/L = -0.05$) cases, and (c) LFC$^{\text{Opt.}}$ case; also showing: (blue lines) the BL displacement thickness, (black lines) the momentum thickness, (black dotted lines) the streamlines, and (white dashed lines) the upstream (x_s/L) and downstream (x_e/L) edges of the LFC slot.

variable x_s. The results clearly indicate that the optimal upstream LFC location coincides with the streamwise position where the perturbations start showing a footprint on the TKE field. Initiating suction at this critical point is essential for effective suppression of the transition mechanism. On the other side, shifting more upstream than the optimal location the LFC slot also results detrimental. This is shown, in terms of friction coefficient, in Fig. 15 and, in terms of TKE field, in Fig. 17(d). In this case, the main drawback is that LFC is implemented too much upstream so, while at the upstream edge of the LFC slot the flow is still relatively stable making suction at that position pointless, at the downstream edge of the LFC slot, the BL disturbances still have room, in terms of streamwise plate extension, to develop enough to cause a pronounced rise of both skin friction (see Fig. 15) and TKE (see Fig. 17).

Overall, these considerations highlight how, for optimal LFC implementations the exact location on BL disturbances activation needs to be known for the different flow condition encountered during flight. At the same time, the LFC embodiment shall be designed with streamwise independent slots such to allow for variable LFC slot extension and position [40].

From Fig. 14(a), it can be observed that the optimal LFC-parameters point lies on the boundary of the feasible domain. As previously discussed, this is typically the case—provided that the suction

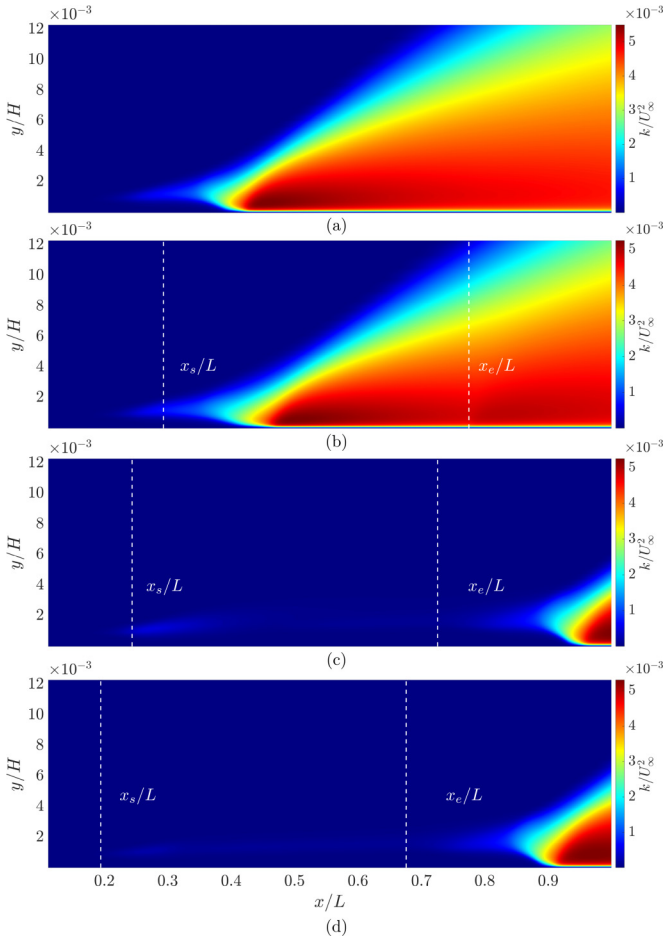

FIG. 17. Turbulent kinetic energy fields for: (a) the natural transition case, (b) LFC$^{\text{Downstr.}}$ ($\Delta x_{\text{LFC}}/L = 0.05$) and (d) LFC$^{\text{Upst.}}$ ($\Delta x_{\text{LFC}}/L = -0.05$) cases, and (c) LFC$^{\text{Opt.}}$ case; also showing: (white dashed lines) the upstream (x_s/L) and downstream (x_e/L) edges of the LFC slot.

velocity is sufficiently high—for the given width of the suction region, d. The bounds imposed by the maximum allowable mass flow rate, $q^{\max}$, however, lead to a different situation. To examine the influence of the mass-flow constraint on the achievable power reduction (PR), a parametric study was conducted considering two suction widths ($d/L = 0.25$ and $d/L = 0.5$) and a range of mass-flow values. For each combination of d/L and q), a one-dimensional optimization of the suction location was performed to determine the maximum achievable PR.

A decomposition of the contributions of W_1, W_2, and W_3 to the total LFC power, W^{total}, for the investigated configurations is presented in Fig. 18. The figure clearly indicates that, for a given suction slot width, there exists an optimal mass flow rate, q^{OPT}, that maximizes PR. Consequently, if $q^{\max} \leqslant q^{\text{OPT}}$, the optimal point lies on the boundary of the feasible domain defined by $q^{\max}$. Conversely, if $q^{\max} > q^{\text{OPT}}$, the optimal design point will lay inside the design space.

Moreover, Fig. 18 illustrates the effect of doubling the volumetric mass flow on W_1, W_2, and W_3. Since W_1/W_N is the complement of the drag reduction (DR), it can be observed—both from Fig. 11 and, to some extent, from Fig. 18—that it plateaus beyond a certain mass flow threshold. Because the reduction of W_1/W_N is the primary contributor to PR, further increases in volumetric mass flow at fixed d/L provide no additional benefit. On the contrary, they become detrimental.

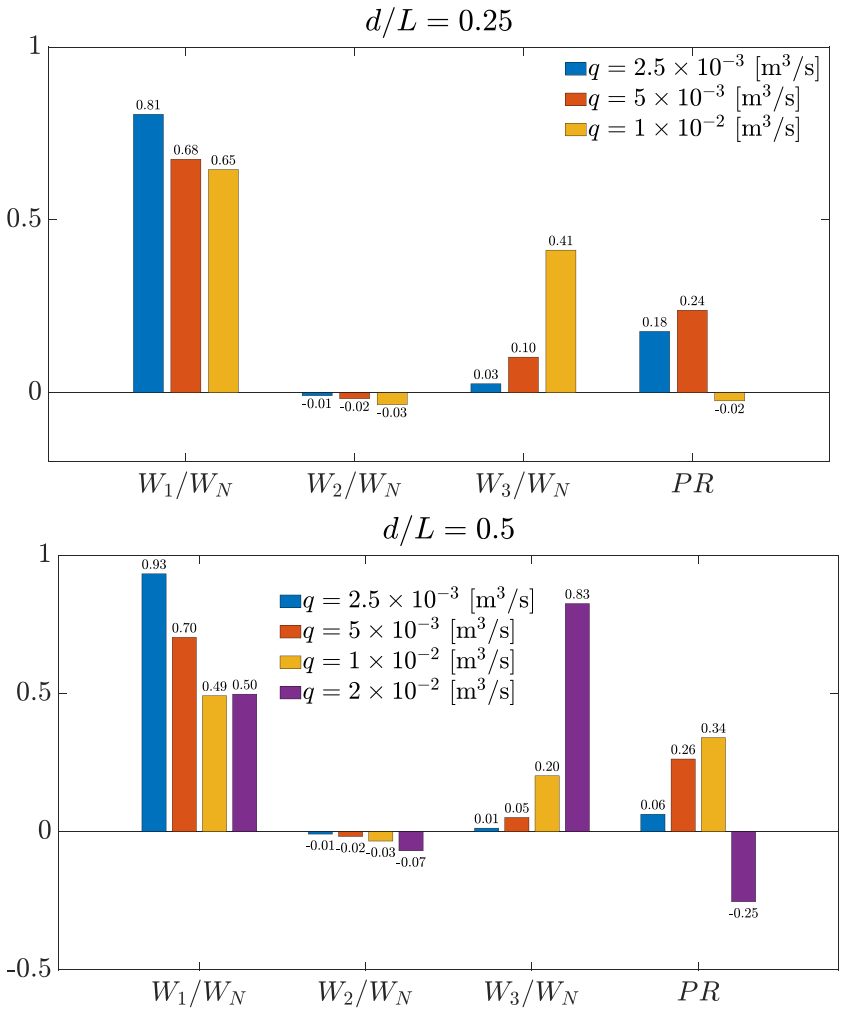

FIG. 18. Bower budget breakdown, considering the Eq. (41) terms, for two different LFC slots widths: (top) $d/L = 0.25$ and (bottom) $d/L = 0.5$, for different values of the mass flow rate (q).

This is because the sensitivity of W_1/W_N to q decreases with increasing q, while the opposite trend holds for W_3/W_N. Specifically, for $d/L = 0.25$, at $q = 1 \times 10^{-2}$ m^3/s (Fig. 18) and, for $d/L = 0.5$, at $q = 2 \times 10^{-2}$ m^3/s (Fig. 18), the gains achieved through drag reduction are entirely offset by the power required to operate the suction system (W_3/W_N) thus leading to negative values of PR.

V. CONCLUSIONS

In this study, we developed a framework for achieving efficient LFC by uniform suction. The proposed framework builds on two main strongholds: (i) the theoretical power budget analysis, thoroughly described in the manuscript; (ii) the combination of a fast, relatively accurate CFD-transition solver coupled with an efficient optimizer.

To develop the proposed framework, we considered the archetypal incompressible, bidimensional, stationary flat plate flow. This flow features a simplified boundary layer transition, usually dominated by streamwise-traveling Tollmien-Schlichting waves, which can be more easily addressed. Besides these considerations, this is the most canonical boundary layer flow, leading to an

assessment of the proposed framework not related to specific geometries and flow configurations. Moreover, the chosen flow is complemented by some more literature as well as by analytical solutions (further exploited in Appendix A).

In this study, first, we examined the predictive accuracy of classical transition models alongside the energetic efficiency of LFC via steady and uniform suction on a flat plate flow. Our investigation aimed to achieve two primary objectives: to validate low-cost computational tools for predicting transition and to identify energy-efficient suction configurations through optimization. We, therefore, assessed the performance of two widely used transition prediction methods—the e^N method and the $\gamma - \mathrm{Re}_\theta$ model—in both natural and suction-controlled boundary layer flows. While both methods accurately predicted the natural transition location, when compared to experimental data, their accuracy significantly decreased in the presence of suction. In particular, the e^N method proved to be unsuited for LFC scenarios, as its prediction of the transition point significantly deviates from the experimental data from Ref. [9]. This discrepancy highlights the limitations of linear stability theory to accurately model the transition process in the presence of suction. A more satisfactory performance is observed with the γ-Re_θ transition model. This model demonstrates good accuracy for lower values of the suction coefficient. However, loss of predictive power emerges for moderate to high suction velocities, where the model starts to diverge from the experimental observations. Nevertheless, the γ-Re_θ model still captures key features of the transition–suction mechanisms and features, such as the slope of the linear region and the location of the inflection point (or "knee") of the curve, as shown in Fig. 9.

Building on this methodological analysis, we then focused on the broader question of LFC energy efficiency. Rather than evaluating suction configurations based solely on drag or transition delay, and inspired by the recent literature on turbulent skin friction control by wall blowing (e.g., Refs. [39,40]), we adopted a comprehensive power-based approach [stronghold (i)]. Based on this approach, we decomposed the total power consumption into three main components: the power required to overcome friction drag (W_1), the minor contribution from the thrust generated by expelling the suction mass flow at velocity U_{jet} (W_2), and the power needed to drive the suction system (W_3). This decomposition enabled us to isolate the tradeoffs inherent of the design of LFC configurations. While suction can effectively reduce friction drag, it can also significantly affect the overall energy budget due to the power required for its operation. If these two aspects are not carefully balanced, unintended and undesirable consequences may arise—most notably, an increase in total energy consumption that would cancel the benefits of laminar flow control.

Finally, to identify optimal suction strategies, we deployed an efficient optimizer (Bayesian optimization, further described in Appendix B) to investigate the efficiency-relevant LFC parameters [stronghold (ii)]. At the end of the optimization process, after assessing 700 different LFC configurations, a maximum power reduction of 34.02 % was achieved. This result stands in contrast to what has been observed in turbulent boundary layer friction drag control, where the use of power as a performance metric typically reveals that neither suction nor blowing leads to an overall reduction in energy consumption [39,40]. In the case of LFC, however, we found that it is indeed possible to attain a net power saving and a very considerable one.

That said, the optimization also revealed that suction configurations must be designed with care. While certain configurations can yield significant power reduction levels, the majority of other LFC configurations have the opposite effect—leading to increased power requirements and undermining the benefits of flow control. This underlines the importance of using optimization frameworks coupled with efficient and relatively accurate CFD-transition solvers explicitly considering energy expenditure, when designing LFC strategies. Similarly, the implementation of LFC should require both reliable flow sensing—to infer the position of the disturbances amplification—and of flow control embodiments featuring variable streamwise extension and position—to account for the different encountered flow conditions. Eventually, LFC deploying non uniform or unsteady suction could also lead to larger power savings. Furthermore, it shall be said that more organized boundary layer disturbances, possibly further amplified by the occurrence of subcritical surface defects, surface roughness, local flow reversal, or other causes likely occurring on aeronautical flows, might

worsen the transition scenario [61]. In other words, either transition would be anticipated [with an impact on the W_I term in Eq. (41)] or a stronger LFC should be deployed (impacting W_{II} and W_{III}) to keep the same transition location. In both these cases, a PR penalization is expected. Nonetheless, the large margins of PR found in this study suggest that efficient LFC could be achieved also for moderately more disturbed flows. If instead critical/supercritical disturbances would affect the boundary layer transition, the effect of LFC is likely much diminished. For these scenarios, in fact, the transition mechanism changes from the canonical modal, linear-first and nonlinear more downstream, disturbance amplification for which LFC is effective, to nonmodal/bypass mechanisms which are much less, if not at all, affected by wall suction [61].

Overall, this study poses the bases for efficient LFC to be then further extended to more realistic and relevant flows, considering the effects of, e.g., pressure gradient, wall curvature, Reynolds and Mach numbers as well as those coming from the development of the boundary layer and of its instabilities along the spanwise direction. All these aspects, nevertheless, go far beyond the scope of the current study and require considerable further research efforts.

ACKNOWLEDGMENTS

This study was carried out within the "WAll-Turbulence Active COntrol" project—funded by European Union—Next Generation EU within the PRIN 2022 PNRR program (D.D.1409 del 14/09/2022 Ministero dell'Università e della Ricerca). G.L.C. was also supported by the GREENER project—funded by the European Union—Next Generation EU within the PRIN 2022 program (D.D. 104-02/02/2022 Ministero dell'Universitá e della Ricerca). This manuscript reflects only the authors' views and opinions and the Ministry cannot be considered responsible for them. The authors acknowledge the support of G. Cafiero to this research.

DATA AVAILABILITY

The data that support the findings of this article are not publicly available. The data are available from the authors upon reasonable request.

APPENDIX A: LFC-LST SOLVER ASSESSMENT

In this Appendix, the developed LFC-LST solver is validated by comparing its results with existing literature. Initially, a comparison was conducted using the conventional LST formulation, i.e., based on the standard OS equation, see Eq. (6) and consider $V(y) = V'(y) = 0$. The amplification rates of the Blasius BL for the same three modes as considered in Refs. [63,64], were computed. A comparison is presented in Table VII, showing a good agreement.

Additionally, the information provided by Fransson and Alfredsson [8] was utilized to further validate the LST solver outputs in terms of eigenfunctions and eigenvalues in LFC scenarios, thus considering a nonzero wall-normal velocity and its first derivative along the wall normal direction ($V(y),\ V'(y) \neq 0$). This was achieved by analyzing the distribution of perturbation amplitudes within the controlled boundary layer, as well as the phase velocity and amplification rate of the perturbations.

TABLE VII. Comparison of literature available and computed amplification rates for the Blasius BL.

Re_{δ^*}	ω	Jordinson [63]	Danabasoglu and Biringen [64]	Current study
336	0.1297	$0.3084 + i\,0.0079$	$0.30864 + i0.00799$	$0.30798 + i0.00807$
598	0.1201	$0.3079 - i0.0019$	$0.30801 - i0.00184$	$0.30748 - i0.00182$
998	0.1122	$0.3086 - i0.0057$	$0.30870 - i0.00564$	$0.30823 - i0.00562$

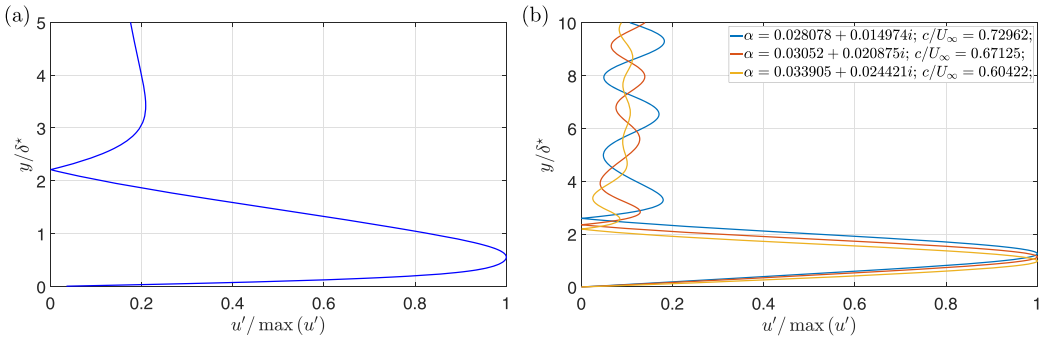

FIG. 19. Normalized wall-normal profile of the perturbation's amplitudes (u'): (a) Blasius BL for $\mathrm{Re}_{\delta^*} = 2443$ and $\omega = 0.0472$ and (b) asymptotic suction BL ($v_w^\star = -1.44 \times 10^{-2}$ m/s) for $\mathrm{Re}_{\delta^*} = 347$ and $\omega = 0.0205$.

In the case without suction, a good agreement was found between the experimental measurements of u', the velocity fluctuations predicted by our LST solver [Fig. 19(a)], and those found by the LST solver of Ref. [8] (see Fig. 20 in the cited paper). However, in the asymptotic suction case, the solutions provided by the two solvers differ. Figure 19(b) illustrates three distinct eigenfunctions computed by the LST for an asymptotic suction profile with $v_w^\star = -1.44 \times 10^{-2}$ m/s (where * is used to denote dimensional quantities) and referred to a mode with $\omega = 0.0205$ (this frequency corresponds to $F = 59$ in Ref. [8] where a different frequency normalization was considered). Among these eigenfunctions, the blue curve was selected, representing the eigenfunction related to the smallest $-\alpha_i$, i.e., the OS spectrum dominating root.

There are two prominent differences between the blue curve in Fig. 19(b) and the curve of Fig. 27 in Ref. [8]. First, the location of the maximum disturbance amplitude differs. In our case, it is approximately at $y/\delta^* \sim 1.3$, whereas, in their case, it was observed at $y/\delta^* \sim 0.7$. Experimental data suggests that the maximum fluctuation within the boundary layer occurs at $y/\delta^* \approx 1.55$. Fransson and Alfredsson [8] discuss a correction in the Re_δ^* value due to an increase in boundary layer thickness, but it is unclear whether the correction was applied solely to the Reynolds number or also to the displacement thickness. If the correction was not applied, adjusting the experimental data ourselves leads to a maximum at $y/\delta^* \approx 1.415$, which is closer to the position of the largest fluctuations predicted by our solver. The most notable difference pertains to the outer-wall tail of u'. The velocity perturbation profiles displayed in Ref. [8] in Fig. 27 exhibit a flat tail with an amplitude of approximately 0.05 % of the maximum amplitude. In contrast, the eigenfunction found by our solver [Fig. 19(b)] shows a sinusoidal behavior with the amplitude of the sinusoid approximately 20% of the maximum amplitude. This oscillatory behavior of the tail could elucidate the scattering of data observed in Ref. [8], with the amplitude of the tail matching well the amplitude of the scattered data, around 20% of the maximum velocity amplitude.

The eigenvalue's experimental imaginary part for this case was $\alpha_i^\star = 0.0153$ mm^{-1}, while the amplification rate found by us is $\alpha_i^\star = 0.0144$ mm^{-1}. Fransson and Alfredsson [8] reported $\alpha_i^\star = 0.0263$ mm^{-1}. Moreover, while the amplification rates align well, the phase velocity calculated by our LST solver shows a significant deviation from the values reported in Ref. [8], both in measurement and theory. Our computed phase velocity is $c/U_\infty = 0.73$, compared to $c/U_\infty = 0.48$ in Ref. [8]. Although the agreement between the LST solver and experimental data is promising, further comparisons are required to bolster confidence on the LST results on the modal dynamics. No additional data sets were found by the authors.

APPENDIX B: BAYESIAN OPTIMIZATION FORMULATION

In this Appendix, we provide an intuitive overview of BO, aimed at acquainting readers, who are new to this method, with its foundational concepts.

Consider the function $f(\boldsymbol{x})$: $\boldsymbol{A} \subseteq \mathbb{R}^d \rightarrow \mathbb{R}$, representative of the physical system under investigation. The system behavior depends on the choice of the design parameters here collected in a vector $\boldsymbol{x} \in \boldsymbol{A}$. We would like to find the design parameters that minimize the function $f(\boldsymbol{x})$:

$$\boldsymbol{x}^{\text{opt}} = \arg\min_{\boldsymbol{x}\in\boldsymbol{A}} f(\boldsymbol{x}). \tag{B1}$$

Although the function $f(\boldsymbol{x})$ is not explicitly known, we can access to its value at any desired point within its domain. This situation can be likened to a black box model; by inputting a specific design configuration into the box, we receive an output $y(\boldsymbol{x}) = f(\boldsymbol{x}) + \epsilon = f(\boldsymbol{x}) + \mathcal{N}(0, \sigma_\epsilon^2)$. This output is the result of a combination of the true system state $f(\boldsymbol{x})$ and a Gaussian distributed noise term that contaminates the acquired information, modeled by $\mathcal{N}(0, \sigma_\epsilon^2)$. To contextualize this further, the black box in question is analogous to the CFD solver. Each time the suction configuration is altered, a simulation is conducted, followed by post-processing that yields the desired quantity $y(\boldsymbol{x})$ for analysis—such as power consumption, drag, or the transition point. The observed noise in this case can be traced back to the residuals of the simulations (which are low but, of course, not zero) or numerical rounding errors.

Returning to the function $f(\boldsymbol{x})$, we model it as a Gaussian process, denoted as $f(\boldsymbol{x}) \sim \mathcal{N}(\boldsymbol{m}(\boldsymbol{x}), \boldsymbol{K}(\boldsymbol{x}, \boldsymbol{x}'))$. This distribution is fully characterized by its mean $\boldsymbol{m}(\boldsymbol{x})$—which represents the expected value of f at the point $\boldsymbol{x}$—and the covariance function $\boldsymbol{K}(\boldsymbol{x}, \boldsymbol{x}')$ which quantifies the covariance between the random variables $\boldsymbol{x}$ and $\boldsymbol{x}'$. Typically, the prior mean function is set to a constant value, which is often zero. The notation $\boldsymbol{K}(\boldsymbol{x}, \boldsymbol{x}')$ encapsulates the dependence between the point $\boldsymbol{x}$ and $\boldsymbol{x}'$. When two random variables exhibit zero covariance, they are considered independent, meaning that knowing the value of one does not influence the probability distribution of the other. In contrast, when two variables exhibit high correlation, the value of one significantly alters the confidence bounds of the other. The covariance matrix is typically modeled using a kernel function (κ), with the choice of the kernel depending on the characteristics of the underlying function f. For example, a periodic kernel can be utilized to impose periodicity on f within a Gaussian process. When the behavior of f is unknown, the radial basis function kernel is often favored due to its inherent flexibility, thus leading to

$$\kappa(\boldsymbol{x}, \boldsymbol{x}') = \sigma_f^2 \exp\left(-\frac{||\boldsymbol{x} - \boldsymbol{x}'||}{2\lambda^2}\right), \tag{B2}$$

where the hyperparameter λ influences the correlation between two adjacent points; a larger λ extends the influence of $\boldsymbol{x}$ further in space. The term σ_f, known as the signal variance, plays a critical role: a smaller value of this parameter results in minimal interdependence among the variables in a multivariate Gaussian process.

Let us suppose that the domain $\boldsymbol{A}$ has already been sampled at n distinct locations, whereby we represent the resulting dataset as $\mathcal{D} = \{(\boldsymbol{x}_i, y_i)\}_{i=1}^n = (\boldsymbol{X}, \boldsymbol{y})$. This dataset contains pairs $(\boldsymbol{x}_i, y_i)$ for each sampled point, effectively encapsulating the available data for analysis. $\boldsymbol{X}$ is the matrix whose rows are the elements of $\boldsymbol{A}$, while $\boldsymbol{y}$ is the vector containing the system's observations. In a Gaussian process, we assume that $f(\boldsymbol{x}_{1:n}) = \boldsymbol{f}$ are jointly Gaussian distributed and the observations $\boldsymbol{y}$ are normally distributed given $\boldsymbol{f}$:

$$\boldsymbol{f}|\boldsymbol{X} \sim \mathcal{N}(\boldsymbol{0}, \boldsymbol{K}), \tag{B3}$$

$$\boldsymbol{y}|\boldsymbol{f}, \sigma_\epsilon^2\boldsymbol{I} \sim \mathcal{N}\big(\boldsymbol{f}, \sigma_\epsilon^2\boldsymbol{I}\big), \tag{B4}$$

where the prior mean function was set to zero ($\boldsymbol{m}(\boldsymbol{X}) = \boldsymbol{0}$) and $K_{i,j} = \kappa(\boldsymbol{x_i}, \boldsymbol{x_j})$. The posterior mean $m(\boldsymbol{x^*})$ and variance $\sigma^2(\boldsymbol{x^*})$, evaluated at any point $\boldsymbol{x^*}$ can be easily calculated using the properties of the multivariate Gaussian distribution of the vector $[\boldsymbol{y}^T,\ y^*]^T$:

$$\begin{bmatrix} \boldsymbol{y} \\ y^* \end{bmatrix} = \mathcal{N}\left(\boldsymbol{0}, \begin{bmatrix} \boldsymbol{K}(\boldsymbol{X}, \boldsymbol{X}) & \boldsymbol{K}(\boldsymbol{X}, \boldsymbol{x^*}) \\ \boldsymbol{K}(\boldsymbol{x^*}, \boldsymbol{X}) & \boldsymbol{K}(\boldsymbol{x^*}, \boldsymbol{x^*}) \end{bmatrix}\right), \tag{B5}$$

which leads to a posterior mean:

$$m(\boldsymbol{x}^*) = \kappa(\boldsymbol{x}^*, \boldsymbol{X})\left[\boldsymbol{K}(\boldsymbol{X}, \boldsymbol{X}) + \sigma_\epsilon^2 \boldsymbol{I}\right]^{-1} \boldsymbol{y}, \tag{B6}$$

and a variance:

$$\sigma^2(\boldsymbol{x}^*) = \kappa(\boldsymbol{x}, \boldsymbol{x}^*) - \kappa(\boldsymbol{x}^*, \boldsymbol{X})\left[\boldsymbol{K}(\boldsymbol{X}, \boldsymbol{X}) + \sigma_\epsilon^2 \boldsymbol{I}\right]^{-1} \kappa(\boldsymbol{X}, \boldsymbol{x}^*). \tag{B7}$$

Hence, at each point $\boldsymbol{x}^*$, the observables y^* is Gaussian distributed around $m(\boldsymbol{x}^*)$ with the variance $\sigma^2(\boldsymbol{x}^*)$:

$$y^* \sim \mathcal{N}(m(\boldsymbol{x}^*), \sigma^2(\boldsymbol{x}^*)). \tag{B8}$$

With an estimate of the expected value and standard deviation of the system's response obtained through the surrogate model, we can now choose and implement an effective sampling policy. The acquisition function, which plays a pivotal role in this strategy, is tasked with selecting the next query point. There exists a wide range of acquisition functions, each engineered to strike its own balance between exploration and exploitation. Exploration is characterized by the function's tendency to probe regions of high uncertainty, while exploitation leverages existing knowledge to focus sampling on areas likely to yield superior outcomes. However, excessive exploration can cause the optimizer to meander aimlessly, thereby slowing convergence. Conversely, excessive exploitation risks the optimization to be stuck in local optima. Thus, finding an effective balance between these two strategies is crucial to optimize BO performance.

In the following paragraph we will delve into only one of the available acquisition functions: the expected improvement. For the expected improvement, we define the improvement function I as

$$I(\boldsymbol{x}^*, y^*, \tau) = -\mathbb{I}(y^* < \tau)(y^* - \tau), \tag{B9}$$

where the function $\mathbb{I}(y^* < \tau)$ has values

$$\mathbb{I}(y^* < \tau) = \begin{cases} 0 & y^* \geqslant \tau, \\ 1 & y^* < \tau, \end{cases} \tag{B10}$$

and τ denotes the threshold that distinguishes an improvement from nonimprovements. Specifically, τ is defined as the best value found during the optimization process: $\tau = \min_{i\in[1,\ldots,n]} y_i$. The expected improvement acquisition function is defined as $\alpha(\boldsymbol{x}) = \mathbb{E}(I)$. Here, a sketch of the demonstration:

$$\begin{aligned} \alpha(\boldsymbol{x}^*) = -\mathbb{E}(I(\boldsymbol{x}^*, y^*, \tau)) &= -\int_{\infty}^{+\infty} \mathbb{I}(y^* < \tau)(y^* - \tau) \frac{\exp\left(-\frac{y^* - \mu(\boldsymbol{x}^*)}{2\sigma(\boldsymbol{x}^*)}\right)}{\sqrt{2\pi}\sigma(\boldsymbol{x}^*)}\, dy^* \\ &= -\int_{\infty}^{+\tau} (y^* - \tau) \frac{\exp\left(-\frac{y^* - \mu(\boldsymbol{x}^*)}{2\sigma(\boldsymbol{x}^*)}\right)}{\sqrt{2\pi}\sigma(\boldsymbol{x}^*)}\, dy^*. \end{aligned} \tag{B11}$$

Making a variable change

$$z = \frac{y^* - \mu(\boldsymbol{x}^*)}{\sigma(\boldsymbol{x}^*)}, \tag{B12}$$

it can be clearly seen that

$$\alpha(\boldsymbol{x}^*) = (\tau - \mu(\boldsymbol{x}^*))\Phi\left(\frac{\tau - \mu(\boldsymbol{x}^*)}{\sigma(\boldsymbol{x}^*)}\right) + \sigma(\boldsymbol{x}^*)\phi\left(\frac{\tau - \mu(\boldsymbol{x}^*)}{\sigma(\boldsymbol{x}^*)}\right). \tag{B13}$$

Finally, the next query point is determined by maximizing the acquisition function. Eligible points include those where there is a substantial improvement, indicated by a large value of $(\tau - \mu(\boldsymbol{x}^*))$, or those characterized by high uncertainty, represented by $\sigma(\boldsymbol{x}^*)$.

[1] N. Beck, T. Landa, A. Seitz, L. Boermans, Y. Liu, and R. Radespiel, Drag reduction by laminar flow control, Energies **11**, 252 (2018).
[2] R. D. Joslin, Aircraft laminar flow control, Annu. Rev. Fluid Mech. **30**, 1 (1998).
[3] K. S. G. Krishnan, O. Bertram, and O. Seibel, Review of hybrid laminar flow control systems, Prog. Aerosp. Sci. **93**, 24 (2017).
[4] J. Svorcan, J. M. Wang, and K. P. Griffin, Current state and future trends in boundary layer control on lifting surfaces, Adv. Mech. Eng. **14**, 16878132221112161 (2022).
[5] J.-P. Marec, Drag reduction: A major task for research, in *Proceedings of the CEAS/DragNet European Drag Reduction Conference on Aerodynamic Drag Reduction Technologies* (Springer, Berlin, 2001), pp. 17–27.
[6] A. L. Braslow, History of suction-type laminar-flow control with emphasis on flight resreach: Monographs in aerospace history number 13, Technical Report, NASA, Washington, D.C. (1999).
[7] G. A. Reynolds and W. S. Saric, Experiments on the stability of the flat-plate boundary layer with suction, AIAA J. **24**, 202 (1986).
[8] J. H. M. Fransson and P. H. Alfredsson, On the disturbance growth in an asymptotic suction boundary layer, J. Fluid Mech. **482**, 51 (2003).
[9] M. Corelli Grappadelli, S. Sattler, P. Scholz, R. Radespiel, and C. Badrya, Experimental investigations of boundary layer transition on a flat plate with suction, in *Proceedings of the AIAA Scitech 2021 Forum* (AIAA, Reston, VA, 2021), p. 1452.
[10] H. L. Meitz and H. F. Fasel, Navier-Stokes simulations of the effects of suction holes on a flat plate boundary layer, Application of Direct and Large Eddy Simulation to Transition and Turbulence, Technical Report ,NASA, Washington, D.C. (1994).
[11] J. A. Masad, A. H. Nayfeh, and A. A. Al-Maaitah, Effect of heat transfer on the stability of compressible boundary layers, Comput. Fluids **21**, 43 (1992).
[12] P. L. O'Sullivan and S. Biringen, Numerical experiments on feedback EMHD control of large scale coherent structures in channel turbulence, Acta Mech. **152**, 9 (2001).
[13] J. Pang and K. S. Choi, Turbulent drag reduction by Lorentz force oscillation, Phys. Fluids **16**, L35 (2004).
[14] S. Grundmann and C. Tropea, Delay of boundary-layer transition using plasma actuators, in *Proceedings of the 46th AIAA Aerospace Sciences Meeting and Exhibit* (AIAA, Reston, VA, 2008), p. 1369.
[15] S. L. Chernyshev, A. P. Kiselev, and A. P. Kuryachii, Laminar flow control research at TsAGI: Past and present, Prog. Aerosp. Sci. **47**, 169 (2011).
[16] J. Serpieri, S. Y. Venkata, and M. Kotsonis, Conditioning of cross-flow instability modes using dielectric barrier discharge plasma actuators, J. Fluid Mech. **833**, 164 (2017).
[17] J. Serpieri and M. Kotsonis, Conditioning of unsteady cross-flow instability modes using dielectric barrier discharge plasma actuators, Exp. Therm Fluid Sci. **93**, 305 (2018).
[18] A. Altıntaş and L. Davidson, Direct numerical simulation analysis of spanwise oscillating Lorentz force in turbulent channel flow at low Reynolds number, Acta Mech. **228**, 1269 (2017).
[19] R. Zhao, C. Y. Wen, X. D. Tian, T. H. Long, and W. Yuan, Numerical simulation of local wall heating and cooling effect on the stability of a hypersonic boundary layer, Int. J. Heat Mass Transf. **121**, 986 (2018).
[20] S. Yadala, M. T. Hehner, J. Serpieri, N. Benard, P. C. Dörr, M. J. Kloker, and M. Kotsonis, Experimental control of swept-wing transition through base-flow modification by plasma actuators, J. Fluid Mech. **844**, R2 (2018).
[21] H. Schlichting and J. Kestin, *Boundary Layer Theory* (Springer, Berlin, 1961), Vol. 121.
[22] P. J. Schmid and D. S. Henningson, *Stability and Transition in Shear Flows* (Springer, New York, NY, 2001), Vol. 142.
[23] H. L. Meitz, Numerical Investigation of Suction in a Transitional Flat-Plate Boundary Layer, Ph.D. thesis, The University of Arizona, 1996.
[24] J. L. Van Ingen, A suggested semi-empirical method for the calculation of the boundary layer transition region, University of Techn., Dept. of Aerospace Eng., Report UTH-74 (1956).
[25] A. Smith and N. Gamberoni, Transition, pressure gradient, and stability theory. Technical Report No. ES. 26388, Douglas Aircraft, El Segundo, CA (1956).

[26] W. W. D. A. Gregory, B. A., Wind-tunnel tests on the 30 per cent symmetrical Griffith aerofoil with distributed suction over the nose, A.R.C. Technical Report 2647 (1953).
[27] W. S. Saric, R. B. Carrillo, and M. S. Reibert, Nonlinear stability and transition in 3-D boundary layers, Meccanica **33**, 469 (1998).
[28] D. Arnal and G. Casalis, Laminar-turbulent transition prediction in three-dimensional flows, Prog. Aerosp. Sci. **36**, 173 (2000).
[29] H. L. Reed and A. H. Nayfeh, Numerical-perturbation technique for stability of flat-plate boundary layers with suction, AIAA J. **24**, 208 (1986).
[30] K. H. Horstmann, G. Redeker, A. Quast, U. Dreßler, and H. Bieler, Flight tests with a natural laminar flow glove on a transport aircraft, Flight Simulation Technologies Conference Exhibit 385 (1990).
[31] G. Schrauf, Large-scale laminar flow tests evaluated with linear stability theory, J. Aircraft **41**, 224 (2012).
[32] R. D. Wagner, D. V. Maddalon, D. W. Bartlett, J. C. F. S., and A. L. Braslow, *Laminar-flow Flight Experiments*, Transonic Symposium: Theory, Application and Experiment, Volume 2 (Springer, Berlin, 1989).
[33] D. G. MacManus and J. A. Eaton, Predictions and observations of the flow field induced by laminar flow control microperforations, Exp. Therm Fluid Sci. **13**, 395 (1996).
[34] D. G. MacManus and J. A. Eaton, Flow physics of discrete boundary layer suction–measurements and predictions, J. Fluid Mech. **417**, 47 (2000).
[35] B. Crowley and C. Atkin, Effect of discrete widely spaced suction on a transitioning flow at high suction rates, in *Proceedings of the 9th IUTAM Symposium on Laminar-Turbulent Transition* (Springer, Berlin, 2022), pp. 359–368.
[36] M. Atzori, R. Vinuesa, G. Fahland, A. Stroh, D. Gatti, B. Frohnapfel, and P. Schlatter, Aerodynamic effects of uniform blowing and suction on a NACA4412 airfoil, Flow, Turbul. Combust. **105**, 735 (2020).
[37] M. Atzori, R. Vinuesa, A. Stroh, D. Gatti, B. Frohnapfel, and P. Schlatter, Uniform blowing and suction applied to nonuniform adverse-pressure-gradient wing boundary layers, Phys. Rev. Fluids **6**, 113904 (2021).
[38] G. Fahland, A. Stroh, B. Frohnapfel, M. Atzori, R. Vinuesa, P. Schlatter, and D. Gatti, Investigation of blowing and suction for turbulent flow control on airfoils, AIAA J. **59**, 4422 (2021).
[39] G. Fahland, M. Atzori, A. Frede, A. Stroh, B. Frohnapfel, and D. Gatti, Drag assessment for boundary layer control schemes with mass injection, Flow, Turbul. Combust. **113**, 119 (2024).
[40] G. Fahland, Airfoil Drag with Uniform Blowing in Turbulent Boundary Layers, Ph.D. thesis, Karlsruher Institut für Technologie (KIT), 2024.
[41] F. Mallor, G. Semprini-Cesari, T. Mukha, S. Rezaeiravesh, and P. Schlatter, Bayesian optimization of wall-normal blowing and suction-based flow control of a NACA 4412 wing profile, Flow, Turbul. Combust. **113**, 93 (2024).
[42] J.-L. Rioual, P. A. Nelson, P. Hackenberg, and O. R. Tutty, Optimum drag balance for boundary-layer suction, J. Aircr. **33**, 435 (1996).
[43] F. R. Menter, R. Langtry, and S. Völker, Transition modelling for general purpose CFD codes, Flow, Turbul. Combust. **77**, 277 (2006).
[44] R. B. Langtry and F. R. Menter, Correlation-based transition modeling for unstructured parallelized computational fluid dynamics codes, AIAA J. **47**, 2894 (2009).
[45] H. B. Keller, *Numerical Solution of Two Point Boundary Value Problems* (SIAM, Philadelphia, PA, 1976).
[46] T. J. Bridges and P. J. Morris, Differential eigenvalue problems in which the parameter appears nonlinearly, J. Comput. Phys. **55**, 437 (1984).
[47] H. Haj-Hariri, Transformations reducing the order of the parameter in differential eigenvalue problems, J. Comput. Phys. **77**, 472 (1988).
[48] S. Motsa and Z. Makukula, On spectral relaxation method approach for steady von Kármán flow of a Reiner-Rivlin fluid with Joule heating, viscous dissipation and suction/injection, Open Physics **11**, 363 (2013).
[49] W. Huang and D. M. Sloan, The pseudospectral method for solving differential eigenvalue problems, J. Comput. Phys. **111**, 399 (1994).

[50] M. V. Morkovin, On the many faces of transition, in *Proceedings of the Symposium on Viscous Drag Reduction* (Springer, Berlin, 1969), pp. 1–31.
[51] T. A. Zaki and P. A. Durbin, Continuous mode transition and the effects of pressure gradient, J. Fluid Mech. **563**, 357 (2006).
[52] NASA, The Langtry-Menter 4-equation transitional SST model, Technical Report ,NASA, Washington, D.C. (2017).
[53] T. Hino, M. Hirota, N. Hirata, and K. Ohashi, Comparison of unstructured grid and overset grid approaches for flow computations around a ship with an energy-saving duct, in *Proceedings of the MARINE VI International Conference on Computational Methods in Marine Engineering* (CIMNE, 2015), pp. 558–567.
[54] W. R. Thompson, On the likelihood that one unknown probability exceeds another in view of the evidence of two samples, Biometrika **25**, 285 (1933).
[55] B. Shahriari, K. Swersky, Z. Wang, R. P. Adams, and N. De Freitas, Taking the human out of the loop: A review of Bayesian optimization, Proc. IEEE **104**, 148 (2015).
[56] A. B. Blanchard, G. Y. C. Maceda, D. Fan, Y. Li, Y. Zhou, B. R. Noack, and T. P. Sapsis, Bayesian optimization for active flow control, Acta Mech. Sin. **37**, 1786 (2021).
[57] Y. Morita, S. Rezaeiravesh, N. Tabatabaei, R. Vinuesa, K. Fukagata, and P. Schlatter, Applying Bayesian optimization with Gaussian process regression to computational fluid dynamics problems, J. Comput. Phys. **449**, 110788 (2022).
[58] The-MathWorks-Inc., Statistics and machine learning toolbox documentation (2022), https://www.mathworks.com/help/stats/index.html.
[59] H. Wedin and S. Cherubini, Permeability models affecting nonlinear stability in the asymptotic suction boundary layer: The Forchheimer versus the Darcy model, Fluid Dyn. Res. **48**, 061411 (2016).
[60] M. Scheffler and P. Colombo, *Cellular Ceramics: Structure, Manufacturing, Properties and Applications* (John Wiley & Sons, 2006).
[61] J. Methel, M. Forte, O. Vermeersch, and G. Casalis, An experimental study on the effects of two-dimensional positive surface defects on the laminar–turbulent transition of a sucked boundary layer, Exp. Fluids **60**, 94 (2019).
[62] B. Egreteau, A. Mure d'Alexis, F. Mery, and C. Davoine, Influence of innovative porous panels for laminar flow control by suction, in *Proceedings of the AIAA Aviation Forum ASCEND 2024* (AIAA, Las Vegas, Nevada, 2024), p. 3760.
[63] R. Jordinson, The flat plate boundary layer. Part 1. Numerical integration of the Orr—Sommerfeld equation, J. Fluid Mech. **43**, 801 (1970).
[64] G. Danabasoglu and S. Biringen, A chebyshev matrix method for the spatial modes of the Orr–Sommerfeld equation, Int. J. Numer. Methods Fluids **11**, 1033 (1990).